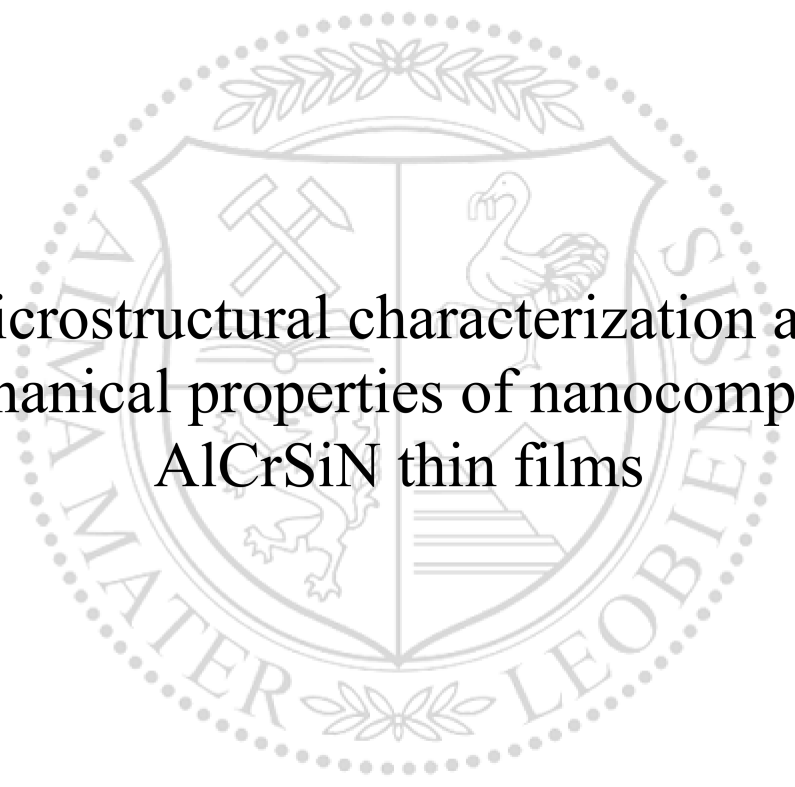




Chair of Materials Physics

Master's Thesis



Microstructural characterization and
mechanical properties of nanocomposite
AlCrSiN thin films

Kevin Kutlesa, BSc

September 2023



EIDESSTÄTLICHE ERKLÄRUNG

Ich erkläre an Eides statt, dass ich diese Arbeit selbständig verfasst, andere als die angegebenen Quellen und Hilfsmittel nicht benutzt, und mich auch sonst keiner unerlaubten Hilfsmittel bedient habe.

Ich erkläre, dass ich die Richtlinien des Senats der Montanuniversität Leoben zu "Gute wissenschaftliche Praxis" gelesen, verstanden und befolgt habe.

Weiters erkläre ich, dass die elektronische und gedruckte Version der eingereichten wissenschaftlichen Abschlussarbeit formal und inhaltlich identisch sind.

Datum 12.09.2023

Unterschrift Verfasser/in
Kevin Kutlesa

Acknowledgments

First and foremost, I want to express my deepest gratitude to my parents, Vlado and Marija, who have always supported me, their remarkable courage and boundless positivity have been a constant source of inspiration for me. Dear Patrik and Tin, I am immensely proud to have you as my brothers, thank you for always being there for me.

I would like to express my gratitude to my supervisor, Jozef Keckes, for entrusting me with this interesting research topic. Beyond that, I am very thankful for the guidance, advice and encouragement he always readily shared with me.

My sincere thanks go to Michael Meindlhumer, whose dedication to providing thorough instructions as well as the attention to detail when reviewing my work significantly contributed to this thesis but also to my personal growth.

I want to thank Sabine Bodner, Nicole Käfer, Juraj Todt, Tobias Ziegelwanger, Atacan Asci and Michael Zawodzki for the numerous insightful and lively conversations, I am thankful to have them as my colleagues and friends.

The TEM analysis would not have been possible without the commitment of Alice Lassnig, I want to thank her for the great contribution to this work.

Special recognition goes to Michael Tkadletz for his expertise in laser processing of lamellae used in synchrotron experiments and to Maximilian Schiester for his support with the heat-treatment of the thin films.

This work has been financially supported by Christian Doppler Research Association. Preparation of the thin film materials was performed by Nikolaus Jäger and Michal Zitek within the scope of the Christian Doppler Laboratory led by Rostislav Daniel. The financial support by the Austrian Federal Ministry for Digital and Economic Affairs and the National Foundation for Research, Technology and Development is gratefully acknowledged.

The provision of synchrotron facilities by the ESRF (European Synchrotron Radiation Facility) for the X-ray nanodiffraction experiments is gratefully acknowledged.

Abstract

Wear-protective hard transition metal nitride (TMN) thin films are distinguished by their superior thermal stability and oxidation resistance coupled with high Young's modulus and remarkable hardness. However, TMNs are inherently brittle materials with typically low toughness. This thesis introduces a multifaceted design approach comprising (i) a nanocomposite AlCrSiN microstructure and (ii) a multilayer architecture, which enables (iii) a controlled precipitation at grain boundaries within specific sublayers. The developed AlCrSiN multilayer film exhibits an extrinsic toughening mechanism, leading to a significant enhancement of fracture resistance.

In this study, two reference monolithic thin films, namely $\text{Al}_{0.63}\text{Cr}_{0.27}\text{Si}_{0.1}\text{N}$ and $\text{Al}_{0.675}\text{Cr}_{0.075}\text{Si}_{0.25}\text{N}$, along with a multilayer thin film, containing alternating sublayers of the two reference materials, were deposited using cathodic arc evaporation. Additionally, a carefully adjusted vacuum heat-treatment at 1050°C for 5 min was applied in order to tailor the microstructure through precipitation. Correlative nanoscale characterization through (i) scanning electron microscopy, (ii) transmission electron microscopy and (iii) cross-sectional synchrotron X-ray nanodiffraction revealed a nanocomposite microstructure composed of wurtzite $\text{Al}(\text{Cr})\text{N}$ and cubic $\text{Cr}(\text{Al})\text{N}$ nanocrystals with sizes of about 5 nm. Heat-treatment led to the precipitation of cubic $\text{Cr}(\text{Al})\text{N}$ in the thin film material with lower Si content, $\text{Al}_{0.63}\text{Cr}_{0.27}\text{Si}_{0.1}\text{N}$, whereas the $\text{Al}_{0.675}\text{Cr}_{0.075}\text{Si}_{0.25}\text{N}$ thin film material remained unaffected by the heat treatment. In the multilayer sample, this led to the alternating occurrence of sublayers with abundant precipitation and sublayers devoid of any precipitation. Mechanical properties were assessed by performing in situ micromechanical tests on freestanding cantilevers fabricated by focused ion beam milling. Unnotched and notched cantilevers were loaded to fracture in order to determine Young's modulus, fracture stress and fracture toughness, respectively. The in-situ observed stepwise crack propagation revealed an unprecedented extrinsic toughening mechanism, which resulted in the significant improvement of the fracture response.

In summary, the correlative analysis of the carefully-designed cross-sectional microstructure and mechanical properties of the AlCrSiN thin films paved the way for the development of a new generation of wear-protective hard thin films with improved fracture behaviour.

Kurzfassung

Verschleißfeste Hartstoffschichten auf der Basis von Übergangsmetallnitriden zeichnen sich durch ihre außerordentliche thermische Stabilität sowie Oxidationsbeständigkeit in Kombination mit hohen elastischen Moduli und Härtewerten aus. Die inhärente Sprödigkeit der Übergangsmetallnitride resultiert jedoch in nachteiligen Zähigkeitseigenschaften. Im Rahmen dieser Arbeit wurde eine (i) Multilagenarchitektur auf der Basis einer (ii) nanokompositen AlCrSiN Mikrostruktur untersucht, in der eine (iii) lagenabhängige Ausscheidungsbildung an Korngrenzen erzielt wurde. Die so entwickelte AlCrSiN Multilagendünnschicht zeigt eine extrinsische Zähigkeitssteigerung, die zu einer signifikanten Erhöhung der Bruchzähigkeit führt.

Untersucht wurden zwei Referenzschichten, $\text{Al}_{0.63}\text{Cr}_{0.27}\text{Si}_{0.1}\text{N}$ und $\text{Al}_{0.675}\text{Cr}_{0.075}\text{Si}_{0.25}\text{N}$, sowie eine Multilagenschicht, die sich aus abwechselnden Lagen der zwei Referenzmaterialien aufbaut. Die Dünnschichten wurden mittels kathodischem Lichtbogenverdampfen abgeschieden und für 5 min bei 1050°C unter Vakuum wärmebehandelt. Nanoskalige Charakterisierung durch (i) Rasterelektronenmikroskopie, (ii) Transmissionselektronenmikroskopie sowie (iii) Röntgen-Nanodiffraktion mit Synchrotronstrahlung zeigen eine nanokomposite Mikrostruktur mit hexagonalen Al(Cr)N und kubischen Cr(Al)N Nanokristalliten mit einer Größe von etwa 5 nm. Die Wärmebehandlung hatte im Dünnschichtmaterial mit niedrigerem Si-Gehalt, $\text{Al}_{0.63}\text{Cr}_{0.27}\text{Si}_{0.1}\text{N}$, die Bildung von kubischen Cr(Al)N Ausscheidungen zur Folge, während $\text{Al}_{0.675}\text{Cr}_{0.075}\text{Si}_{0.25}\text{N}$ ausscheidungsfrei blieb. In der Multilagenschicht führte das zu einer alternierenden Abfolge an Zwischenlagen mit und ohne Ausscheidungsbildung. Mechanische Eigenschaften wurden mittels in situ Biegeversuchen an freistehenden Mikrobiegebalken bestimmt, die durch fokussierte Ionenstrahlmikroskopie hergestellt wurden. Elastizitätsmodul und Bruchspannung wurden durch Versuche an ungekerbten Biegebalken gemessen, Versuche an gekerbten Biegebalken ermöglichten die Bestimmung der Bruchzähigkeit. Die in situ beobachtete schrittweise Rissausbreitung deckte eine extrinsische Zähigkeitssteigerung auf, die in einer signifikanten Verbesserung des Bruchverhaltens resultiert.

Die korrelative Analyse der gezielt eingestellten Mikrostruktur und Messung der mechanischen Eigenschaften der AlCrSiN Dünnschichten tragen maßgeblich zur Entwicklung einer neuen Generation an verschleißfesten Hartstoffschichten mit verbesserten Zähigkeitseigenschaften bei

Contents

Affidavit	II
Acknowledgments	III
Abstract	IV
Kurzfassung	V
1 Introduction	1
1.1 Nature and limitation of wear-resistant thin films	1
1.2 Synthesis strategies to alter microstructure and fracture toughness	1
1.3 Nanocomposite AlCrN thin films	2
1.3.1 Foundations of $\text{Al}_x\text{Cr}_{1-x}\text{N}$ thin films	2
1.3.2 Influence of Si addition on microstructure and properties of $\text{Al}_x\text{Cr}_{1-x}\text{N}$ thin films	4
1.4 Objective and scope of this work	5
2 Experimental methods	7
2.1 Thin film synthesis	7
2.1.1 Deposition by cathodic arc evaporation	7
2.1.2 Synthesis and architecture of the investigated AlCrSiN thin films	8
2.1.3 Tailoring the microstructure through heat-treatment	9
2.2 Scanning electron microscopy	10
2.3 Transmission electron microscopy	10
2.4 Characterization by cross-sectional X-ray nanodiffraction	10
2.4.1 Bragg condition for constructive interference of X-rays	10
2.4.2 Cross-sectional X-ray nanodiffraction at synchrotron sources	12
2.4.3 Phase and texture analysis from collected Debye-Scherrer rings	13
2.4.4 Microstructure analysis from peak broadening	14
2.4.5 Residual stress characterization	14
2.5 Sample preparation by focused ion beam micromachining	17
2.5.1 Polishing cross-sections-with a focused ion beam	17
2.5.2 Fabrication of microcantilevers with a focused ion beam	18
2.6 Micromechanical <i>in situ</i> bending tests	19
2.6.1 <i>in situ</i> testing in a scanning electron microscope	19

2.6.2	Evaluation of Young's modulus	22
2.6.3	Fracture stress evaluation	23
2.6.4	Fracture toughness evaluation	23
2.6.5	Analytical solution for the determination of crack lengths	24
3	Results	26
3.1	SEM Analysis of thin film morphology and microstructure	26
3.2	TEM characterization of microstructure and chemical properties	28
3.2.1	Al _{0.63} Cr _{0.27} Si _{0.1} N monolithic thin film	29
3.2.2	Al _{0.675} Cr _{0.075} Si _{0.25} N monolithic thin film	30
3.2.3	AlCrSiN multilayer thin film	30
3.3	Cross-sectional X-ray nanodiffraction measurements	32
3.3.1	Al _{0.63} Cr _{0.27} Si _{0.1} N monolithic thin film	33
3.3.2	Al _{0.675} Cr _{0.075} Si _{0.25} N monolithic thin film	35
3.3.3	AlCrSiN multilayer thin film	37
3.4	Mechanical properties obtained by <i>in situ</i> microcantilever bending	40
3.4.1	Characterization of Young's modulus, fracture stress and fracture toughness	40
3.4.2	Qualitative analysis of the fracture surfaces after microcantilever bending	44
3.4.3	Evaluation of stepwise crack propagation in the heat-treated Al-CrSiN multilayer	47
4	Discussion	51
4.1	Microstructural evolution of the thin films upon heat-treatment	51
4.2	Extrinsic toughening by sequential application of precipitation-based grain boundary design	52
5	Conclusions and outlook	55
	Bibliography	56
	List of Figures	62
	List of Tables	68

1

Introduction

1.1 Nature and limitation of wear-resistant thin films

Due to the unique interplay of metallic, ionic and covalent chemical bonding, transition metal nitride (TMN) thin films demonstrate exceptional physical attributes, including (i) remarkable hardness, (ii) elevated Young's modulus, (iii) outstanding abrasion resistance and (iv) favourable oxidation resistance, coupled with (v) exceptional thermal stability [1–5]. This favourable combination of properties relevant to various applications has led to their widespread use in demanding industrial applications, such as protective thin films on casting and cutting tools, as well as thermal and diffusion barriers in mechanical and electronic components [1, 2, 6]. Albeit for the aforementioned advantageous properties, the performance of these hard ceramic thin films is however often overshadowed by their low fracture stress and fracture toughness [7].

In order to enhance the mechanical properties of TMN thin films, the TMN research community has proposed and experimentally evaluated various toughening concepts [8–13]. By intentionally designing thin films to incorporate carefully selected sub-layers, interfaces, precipitates, grain boundaries, residual stress gradients and diverse non-stoichiometric phases with distinct physical properties, there is still the potential to significantly enhance the comprehensive physical characteristics of TMN films [2, 6]. The transition towards a new generation of wear-resistant thin films involves a combining of well-established mechanisms for enhancing toughness with innovative microstructural design strategies. This integration is anticipated to raise the energy threshold necessary for crack initiation and propagation [7].

1.2 Synthesis strategies to alter microstructure and fracture toughness

The constraints imposed by low fracture stress and toughness can be attributed mainly to fracture along columnar grain boundaries of low cohesive energy [7, 9]. This gives

rise to intercolumnar fracture behaviour under the application of mechanical loads. To date, various strategies have been devised to bridge the gap between hard and tough protective thin films.

One of these strategies involves elemental alloying, leading to the formation of innovative supersaturated solid solutions that enhance the intrinsic toughness [8, 14, 15]. Other approaches are based on extrinsic toughening mechanisms designed to influence crack propagation [7, 9, 16]. Biological materials, such as nacre [17] or bone [18] can serve as model material systems for increasing toughness of brittle materials, by hierarchical structuring of hard ceramic and soft biopolymer layers combining high stiffness with damage tolerance [19, 20]. As demonstrated by Kolednik *et al.* in such biocomposites, often referred to as brick-and-mortar structures, the reduction in Young's modulus in the thin soft layers results in a significant decrease in the crack driving force and concurrent crack arrest [21].

Similarly, in protective thin films, toughening can be achieved by applying multilayer thin films composed of periodically alternating layers with distinct mechanical properties [10]. In this case, progressing cross-sectional cracks are either deflected or terminated at layer interfaces, allowing for stress relaxation through plastic deformation in the softer layers [16]. The combination of sculptured growth with multilayer arrangement of hard and soft layers can lead to further strengthening and toughening of the thin films, as shown by Daniel *et al.* [9, 22]. Additionally, when the dimensions of the multilayers are reduced to nanometre-scale periodicity lengths, so-called superlattice structures can be constructed [23]. The observed increase in fracture toughness may be attributed to the compositional fluctuations within the nanoscale bilayers, resulting in spatially oscillating elastic moduli that, in turn, influence crack growth [12, 23].

In summary, it can be concluded that the multilayered microstructure is expected to impede crack propagation, leading to improved strength and fracture toughness properties [20, 22].

1.3 Nanocomposite AlCrN thin films

1.3.1 Foundations of $\text{Al}_x\text{Cr}_{1-x}\text{N}$ thin films

The addition of Al to transition metal nitrides such as TiN and CrN, which had already been established in the 1980s, was driven by the need to enhance oxidation stability while simultaneously increasing hardness and wear resistance [2, 24, 25]. Indeed, the formation of a mixed $\text{Cr}_2\text{O}_3\text{-Al}_2\text{O}_3$ layer on the film surface acts as an effective protective barrier against further decomposition of the metastable $\text{Al}_x\text{Cr}_{1-x}\text{N}$ solid solution during exposure

to high temperatures, resulting in oxidation onset temperatures surpassing 1000°C [26, 27].

Despite the above-mentioned beneficial property enhancement of the addition of Al to CrN [25], the deposition of a $\text{Al}_x\text{Cr}_{1-x}\text{N}$ thin film generally results in the formation of a thermodynamically metastable solid solution. Up to a critical aluminium solubility limit of $x = 0.75$, a face centred cubic lattice forms with Al atoms substituting the Cr atoms in a B1 structure (c-Cr(Al)N). Al contents exceeding this solubility limit lead to the formation of wurtzite B4 Al(Cr)N (w-Al(Cr)N) crystal structure, with Al atoms now replaced by Cr atoms [28–30]. Thin films in the transition region around $x = 0.75$ do not exhibit a sharp switch between the two crystal structures but rather a mixture of cubic and segregated wurtzite grains [30, 31]. In metastable solid solutions, elevated temperatures trigger phase transformations towards thermodynamic equilibrium. Therefore, during the thermal loading of cubic $\text{Al}_x\text{Cr}_{1-x}\text{N}$ thin films, the formation of w-AlN precipitates is observed [30]. Upon further thermal loading, the Cr-enriched cubic matrix then decomposes to Cr via an intermediate step involving Cr_2N , releasing gaseous N_2 in the process [29]. On the other hand, the annealing of wurtzite $\text{Al}_x\text{Cr}_{1-x}\text{N}$ leads to the formation of c-CrN precipitates within the w-Al(Cr)N matrix, which, in turn, undergo the decomposition pathway described above, ultimately transforming into Cr while releasing N_2 [13]. In the latter case, the decomposition of CrN occurs at higher temperatures because the precipitates are embedded in an Al-enriched matrix that inhibits the diffusion of Cr atoms [32].

Exact determination of the crystal structure and thermally activated processes in the $\text{Al}_x\text{Cr}_{1-x}\text{N}$ thin films is of significant importance for understanding their functional properties. Firstly, notable differences exist in the mechanical properties between w-Al(Cr)N and c-Cr(Al)N. Experimental data indicate higher hardness and stiffness for the cubic phase compared to the wurtzite phase [25, 33]. Secondly, and pivotal to this work, Meindlhumer et al. have shown for a w- $\text{Al}_{0.9}\text{Cr}_{0.1}\text{N}$ thin film that it is possible to significantly improve its mechanical behaviour by harnessing the potential of precipitation-based grain boundary design [13]. In detail, vacuum annealing of w- $\text{Al}_{0.9}\text{Cr}_{0.1}\text{N}$ at 1100°C resulted in the formation of cubic CrN precipitates, altering the fracture mechanism from inter- to trans-granular and concomitantly increasing Young’s modulus, hardness, fracture strength and fracture toughness.

1.3.2 Influence of Si addition on microstructure and properties of $\text{Al}_x\text{Cr}_{1-x}\text{N}$ thin films

The addition of a substantial amount of Si into the metastable solid solution of $\text{Al}_x\text{Cr}_{1-x}\text{N}$ promotes the formation of a nanocomposite microstructure [30, 34–36]. The incorporation of Si into the crystalline phase is suppressed and the atoms segregate at the grain boundaries, instantiating the formation of a segmented phase. The resultant composite microstructure comprises a nanocrystalline phase consisting of *w*-Al(Cr)N and *c*-Cr(Al)N crystallites of 3-5 nm in size, embedded within an amorphous tissue phase composed of Si_xN_y (*a*- Si_xN_y) spanning only a few atomic layers (<1 nm) [27, 34].

As discussed previously *c*-Cr(Al)N remains stable up to $x = 0.75$ in ternary $\text{Al}_x\text{Cr}_{1-x}\text{N}$ thin films. However, in the Si-induced nanocomposite, a dual-phase crystalline structure comprising *c*-Cr(Al)N and *w*-Al(Cr)N is observed for Al contents below ~65 at.% [34]. The emergence of the hexagonal phase can be attributed to several factors. Density functional theory (DFT) calculations carried out for $\text{Al}_x\text{Ti}_{1-x}\text{N}$ thin films have revealed a crystallite size-dependent phase stabilization, where decreasing grain sizes lead to a destabilization of the respective cubic phase [37]. Apart from that, the similarity between the Al-N and Si-N bonds, both characterized by strong covalent chemical bonding in contrast to the metallic bonding character of Cr-N, could explain why Si addition promotes the formation of *w*-Al(Cr)N [38]. In principle, the presence of the wurtzite phase can be considered advantageous as it facilitates grain boundary segregation upon heat-treatment, with the corresponding effects on the thin film properties described in the previous section 1.3.1.

At the length scale of the nanocomposite microstructure, size effects must be taken into account when interpreting mechanical properties. In fact, dislocation-driven plasticity is negligible in the nanosized crystallites [39] and hindered at grain boundaries as well as at the interface between the crystallites and the amorphous tissue [34, 40]. Additionally, the low thickness of the intermediate amorphous Si_xN_y interlayer prevents grain boundary sliding and, consequently, plastic deformation. As a result, the presence of the nanocomposite microstructure is accompanied also by elevated hardness values [2]. Bartosik et al. have reported increasing hardness and fracture toughness for nanocomposite Ti-Si-N thin films with increasing Si content, peaking at 10 and 8.5 at.% Si, respectively [41].

In addition to the favourable mechanical properties, the nanocomposite approach concurrently improves the thermal stability of thin films. Under operating conditions such as dry or high-speed cutting, protective thin films on cutting tools must withstand temperatures exceeding 1000°C [42]. In these temperature ranges, nitrogen diffusion is

necessary for the thermally induced decomposition described above. However, the strong and dense a-Si_xN_y interface inhibits the nitrogen diffusion along grain boundaries, suppressing the decomposition process and thereby improving thermal stability [34].

Furthermore, the amorphous Si_xN_y intergranular boundary phase in the nanocomposite structure decisively contributes to oxidation stability [43, 44]. As proposed in Ref. [42], a very effective way to retard oxidation processes in thin films is the introduction of an amorphous phase that interrupts the continuous connection between the crystalline phases and substantially hinders oxygen migration.

1.4 Objective and scope of this work

The main objective of this work is to explore a potential for enhancing the fracture behaviour of a TMN thin film by employing (i) a multilayer film morphology based on (ii) a Al_xCr_ySi_zN nanocomposite microstructure, while also exploiting (iii) a precipitation-based grain boundary design.

To achieve this objective, *three thin films* with three distinct compositions were examined. A multilayer consisting of intermittent layers with Si contents of $z = 0.1$ and $z = 0.25$ was deposited by cathodic arc evaporation. For comparison, also two reference thin films of the same composition as the individual sublayers of the multilayer, namely Al_{0.63}Cr_{0.27}Si_{0.1}N and Al_{0.675}Cr_{0.075}Si_{0.25}N, were prepared in the form of monolayers. All three prepared samples were subjected to a heat-treatment at 1050°C for 5 minutes. The thin film with lower Si content is expected to form globular c-CrN precipitates upon heat-treatment, whereas the microstructure of the high-Si containing thin film should remain unaffected. Heat-treatment of the multilayer thin film should yield a cross-sectional pattern of alternating sublayers, some containing precipitates and others without.

In order to analyse the relationship between the nanocomposite Al_xCr_ySi_zN microstructure and composition on one hand, and the mechanical properties of the thin films on the other, a correlative analysis was carried out at the nanoscale level. The multilayer as well as the two reference thin films were analysed in both as-deposited and heat-treated conditions.

Qualitative microstructural analysis of the thin film's architecture was performed using scanning electron microscopy (SEM) on fracture cross-sections and focused ion beam (FIB) polished cross-sections. Additionally, transmission electron microscopy (TEM) analysis was carried out in combination with energy dispersive X-ray spectroscopy (EDS) for a comprehensive nanoscale characterisation of the nanocomposite AlCrSiN thin films. The microstructural evaluation clearly proved the presence and absence of precipitations in the low and high Si-containing thin films after annealing, respectively.

Complementary cross-sectional X-ray nanodiffraction (CSnanoXRD) using synchrotron radiation was used to gain qualitative and quantitative insight into the cross-sectional variation of the thin film (i) phases, (ii) texture, (iii) microstructure and (iv) residual stresses.

To assess the micromechanical properties of the thin films, in situ micromechanical tests were carried out on freestanding cantilevers produced by FIB milling on all three investigated thin films in both as-deposited and heat-treated conditions. Unnotched and notched cantilevers were prepared for each specimen, allowing assessment of Young's modulus and fracture stress as well as fracture toughness, respectively. After the in situ testing, morphology of fracture surfaces of the tested cantilevers was evaluated ex situ in the SEM.

In the case of the annealed multilayer specimens, the recorded load-displacement curves exhibited a significant load drop with a concomitant reduction in stiffness that was associated to a stepwise crack propagation. The measured change in stiffness allowed for an analytical evaluation of the crack length in the microcantilever. The results were correlated with ex situ fractography in the SEM and confirmed crack arrest at the high Si-containing interfaces of the multilayered thin films.

The correlation of the applied nanoscale characterization methods facilitates the understanding of the influence of microstructure, elemental composition and thermal history on the mechanical properties of the investigated thin film materials. This paves the way for the development of a new generation of wear-resistant hard thin films applying extrinsic toughening based on the sequential application of precipitation-based grain boundary design.

2

Experimental methods

2.1 Thin film synthesis

2.1.1 Deposition by cathodic arc evaporation

Currently, the most widely used technique for the deposition of hard protective thin films is cathodic arc evaporation [2]. As the name implies, the thermal energy to vaporise the target material is induced by a low voltage (10^1 to 10^2 V) and high current (10^2 to 10^3 A) arc discharge [45]. As a result, a non-stationary discharge spot with high current densities is formed above the cathode surface, which in turn leads to the creation of a plasma with ionisation rates up to 100% [2]. With the target acting as a cathode, metal ions from the plasma are accelerated towards the target material, where subsequent high-energy impacts eject neutral metal vapour metal ions as well as microdroplets as shown in Fig. 2.1.

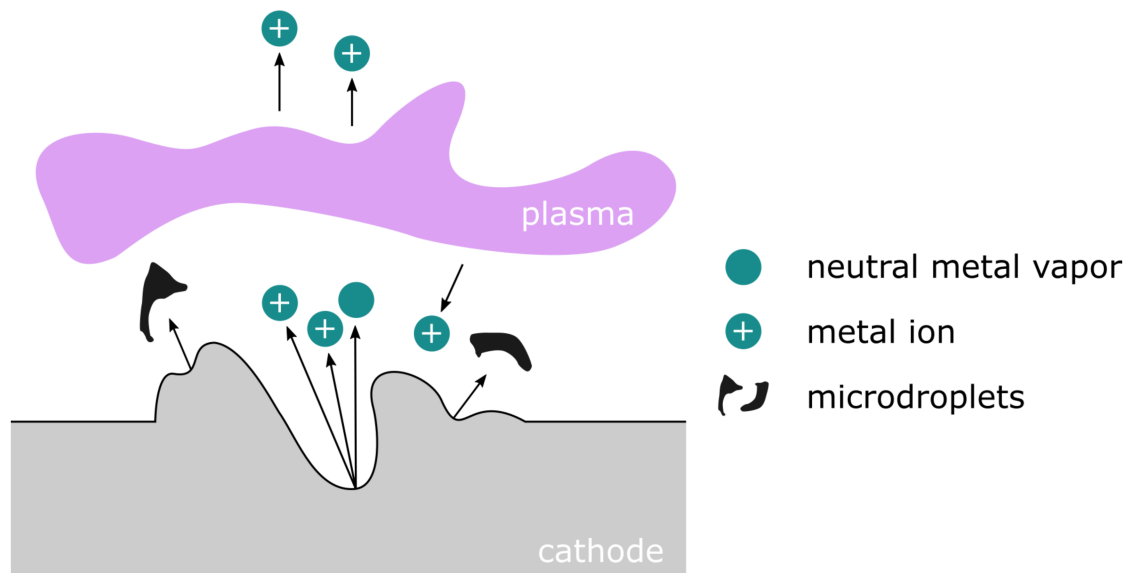


Figure 2.1: Schematic overview of the sputter processes taking place at the target surface during cathodic arc evaporation, redrawn after [45].

The vaporised target atoms travel to the substrate where they condense and remain attached. As is common with physical vapour deposition (PVD) processes, only those parts of the substrate that are exposed to the target are coated. If a reactive gas, such as N_2 , is injected into the thin film chamber, the vaporised target atoms can react with the gas to form nitrides, which are then deposited on the substrate [2].

2.1.2 Synthesis and architecture of the investigated AlCrSiN thin films

In this work, three different AlCrSiN thin films with different Si contents were synthesised using an industrial size alpha 400P deposition system from voestalpine eifeler-Vacotec. Mirror polished tungsten carbide (WC-Co, 6 wt.% Co) cylinders with a diameter of 20 mm and a thickness of 5 mm were used as substrate material. Prior to the deposition of the thin films, the substrates were heated and plasma-etched for adhesion-promoting surface activation. All three thin films were deposited in a pure reactive nitrogen atmosphere at a pressure of 4 Pa, the substrate temperature was 480°C, while the arc current and substrate bias voltage were kept constant at 100 A and 100 V, respectively. Uniform rotation of the substrate carousel at 2 rpm ensured homogeneous deposition of the thin film with a target-to-substrate distance of approximately 100 mm. Prior to the deposition of the AlCrSiN layers, an adhesion layer of TiN with a thickness of ~200 nm was deposited. After the deposition of the TiN adhesion layer, the AlCrSiN layers were deposited. Two reference thin films were deposited from $Al_{0.63}Cr_{0.27}Si_{0.1}$ and $Al_{0.675}Cr_{0.075}Si_{0.25}$ cathodes. The former thin film material with lower Si content is already known to form precipitates after annealing at 1050°C [46]. For the multilayer thin film, the two reference materials were periodically alternated, resulting in a multilayer structure consisting of 10 periods of 250 nm thick layers of $Al_{0.63}Cr_{0.27}Si_{0.1}N$ followed by 50 nm thick layers of $Al_{0.675}Cr_{0.075}Si_{0.25}N$ as schematically shown in Fig. 2.2.

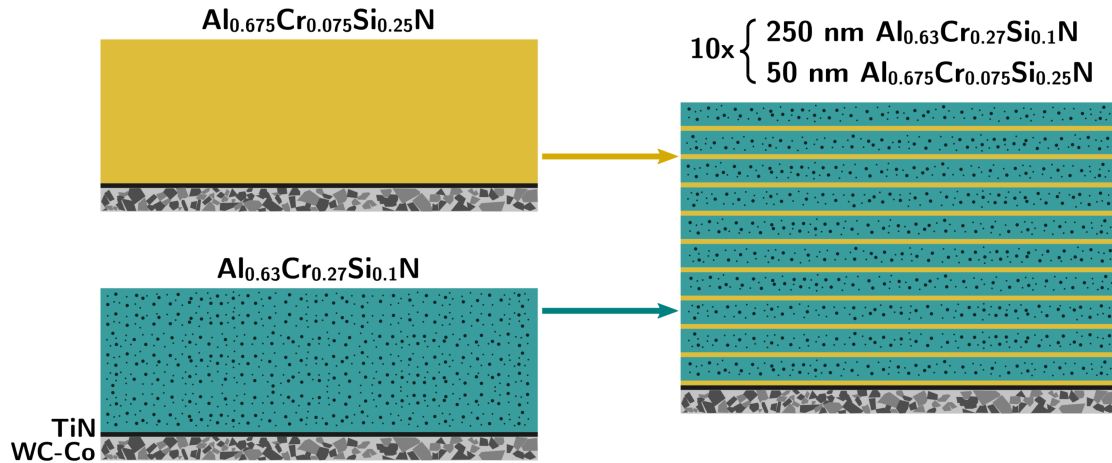


Figure 2.2: Schematic representation of the three investigated thin films, note that this sketch is not true to scale. In the $\text{Al}_{0.63}\text{Cr}_{0.27}\text{Si}_{0.1}\text{N}$ thin film the heat-treatment leads to the formation of globular $c\text{-Cr}(\text{Al})\text{N}$ precipitates, while the second reference thin film $\text{Al}_{0.675}\text{Cr}_{0.075}\text{Si}_{0.25}\text{N}$ is expected to remain unaffected by the heat-treatment.

2.1.3 Tailoring the microstructure through heat-treatment

In this work, all three thin film types were annealed in a vacuum furnace at 1050°C for 5 min. The aim of the heat-treatment was to initiate a formation of precipitates only in the thin film material with lower Si content. In the multilayer structure, the heat-treatment is expected to lead to the creation of alternating sublayers containing precipitates and those lacking them, subsequently inducing both trans-and intergranular fracture patterns [13]. An overview of the analysed thin films is given in Table 2.1.

Table 2.1: An overview of the three deposited thin films and the applied annealing conditions. Altogether six sample types were analysed in this thesis.

cathode composition	sample name	investigated composition
$(\text{Al}_{0.7}\text{Cr}_{0.3})_{0.9}\text{Si}_{0.1}$	$\text{Al}_{0.63}\text{Cr}_{0.27}\text{Si}_{0.1}\text{N}$	as-deposited
		1050°C for 5 min
$(\text{Al}_{0.9}\text{Cr}_{0.1})_{0.75}\text{Si}_{0.25}$	$\text{Al}_{0.675}\text{Cr}_{0.075}\text{Si}_{0.25}\text{N}$	as-deposited
		1050°C for 5 min
10 x sublayers of 250 nm $(\text{Al}_{0.7}\text{Cr}_{0.3})_{0.9}\text{Si}_{0.1}$ 50 nm $(\text{Al}_{0.9}\text{Cr}_{0.1})_{0.75}\text{Si}_{0.25}$	AlCrSiN multilayer	as-deposited
		1050°C for 5 min

2.2 Scanning electron microscopy

Scanning electron microscopy (SEM) was carried out in a Zeiss LEO 1525 using an acceleration voltage of 3 kV, aperture sizes of 20 and 30 μm and the in-lens secondary electron (SE) detector. SEM with the above-mentioned parameters was used for analysis of (i) fractured cross-sections (ii) FIB-polished cross-sections and the imaging of (iii) microcantilevers prior to the *in situ* testing and (iv) fracture surfaces of the tested cantilevers. Post-processing of the acquired SEM micrographs, *i.e.* adjustment of brightness and contrast, was performed with the open source software ImageJ [47].

2.3 Transmission electron microscopy

The aim of the TEM analysis was to identify the formation and morphology of precipitates as an effect of the specific annealing treatment. Therefore, cross-sectional electron beam-transparent lamellae were prepared by a FEI Helios NanoLab 660 FIB with progressively decreasing voltages and ion currents of the Ga^+ -ion source from 30 to 2 kV and 40 nA to 50 pA, respectively. The microstructure of the heat-treated samples was analysed in a JEOL JEM-2200F, high-angle annular dark-field imaging (HAADF) was carried out in scanning transmission electron microscopy (STEM) mode. The TEM analysis also included a spatially-resolved evaluation of the thin film elemental composition by energy dispersive X-ray spectroscopy (EDS), performed with the integrated Oxford INCA Energy TEM 200 EDX system.

2.4 Characterization by cross-sectional X-ray nanodiffraction

Cross-sectional X-ray nanodiffraction, as a relatively novel synchrotron technique, has been proven viable for characterising gradients of crystalline phases, texture, microstructure and residual stresses in thin films with nanoscale resolution [48, 49]. In this chapter, a brief introduction to X-ray diffraction in general and in particular of cross-sectional X-ray nanodiffraction (CSnanoXRD) is given.

2.4.1 Bragg condition for constructive interference of X-rays

X-rays are electromagnetic waves with a wavelength in the order of $\sim 1 \text{ \AA}$. Due to the X-ray wavelength being comparable to the atomic distances within a common crystal, the interaction of X-rays with the crystal gives rise to the presence of interference maxima and minima. These phenomena are characterized by the term “X-ray diffraction”. During an experiment, incident X-rays are scattered by the electron shells of the atoms

in a crystal as indicated in Fig. 2.3. The condition for constructive interference and occurrence of X-ray maxima is given by the Bragg equation [50]:

$$n\lambda = 2d \sin \theta, \quad (2.1)$$

where λ is the wavelength, d is the spacing of the lattice planes, θ is the Bragg angle at which the incident beam is reflected and n is an integer indicating the order of the diffracted peak.

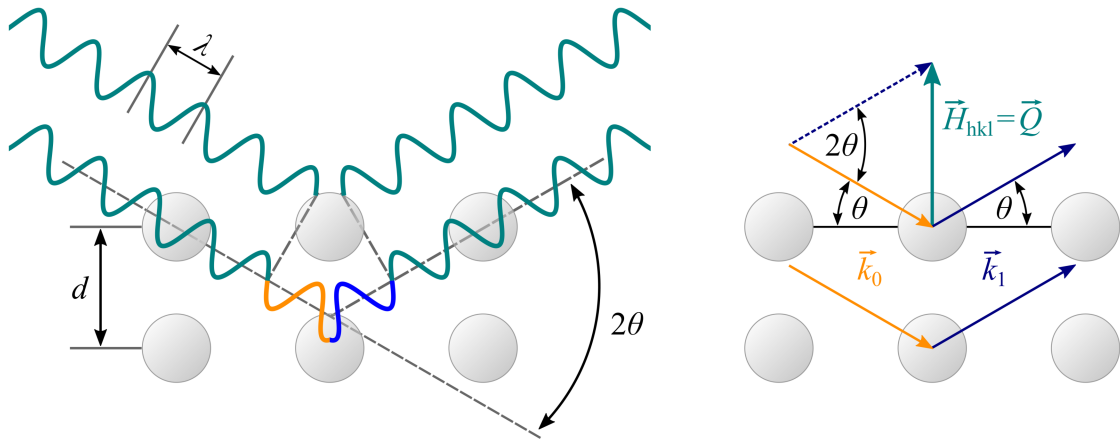


Figure 2.3: Constructive interference occurs when the path difference between two interfering waves is an integer multiple of the wavelength λ . Since the waves are elastically scattered, the wavelength remains constant. The right-hand figure shows the condition of interference transferred to reciprocal space. Diffraction is only recorded if the diffraction vector \vec{Q} is equal to the reciprocal space vector \vec{H}_{hkl} . \vec{k}_0 and \vec{k}_1 represent primary and secondary beam vectors, respectively.

If the Bragg condition is fulfilled, the X-rays are reflected by a parallel set of lattice planes (hkl). Expressing this constructive interference condition with the help of the reciprocal space concept, we see that the reciprocal space vector \vec{H}_{hkl} must coincide with the diffraction vector \vec{Q} for a beam to be diffracted.

$$\vec{Q} = \vec{H}_{hkl}, \quad (2.2)$$

$$|\vec{H}_{hkl}| = \frac{1}{d_{hkl}}, \quad (2.3)$$

$$\vec{Q} = \vec{k}_1 - \vec{k}_0, \quad (2.4)$$

2.4.2 Cross-sectional X-ray nanodiffraction at synchrotron sources

In addition to conventional X-ray experiments in laboratory, synchrotron radiation generated at research facilities such as the European Synchrotron Radiation Facility (ESRF) in Grenoble can be used for advanced material characterisation. Synchrotron measurements combine the major advantages of an X-ray source with high photon flux density, high-precision sample positioning and sophisticated optics that allow nanofocusing of the X-ray beam [51]. Thus, the requirements for the cross-sectional investigation of thin films with thicknesses in the micrometre range are met. Keckes *et al.* developed the method of cross-sectional X-ray nanodiffraction (CSnanoXRD), where scans are performed in transmission geometry with a beam oriented parallel to the film-substrate interface, a schematic of the experiment is given in Fig. 2.4 [49]. The monochromatic synchrotron X-ray beam can be focused down to ~ 30 nm [52] using multilayer Laue lenses (MLL). Diffraction in polycrystalline samples leads to Debye-Scherrer rings that are collected with a 2D detector. A radial slice through a Debye-Scherrer ring produces an intensity versus 2θ plot as known from laboratory XRD measurements. The position, intensity, peak width and shape of the recorded diffraction patterns contain the desired information on crystalline phases, texture, domain size and residual stresses in the sample being measured.

CSnanoXRD measurements were performed at the ESRF ID13 beamline with a beam size of approximately 75×75 nm². Thin cross-sectional lamellae with a thickness of ~ 50 μ m were scanned with a step size of 50 nm. An EigerX 4M Hybrid Photon Counting (HPC) detector was used to collect the two-dimensional diffraction patterns. Comprehensive data analysis was performed using the *pyFAI* software package [53, 54]. The measurements were performed at two beamlines, for the as-deposited multilayer and both as-deposited and heat-treated monolayer $\text{Al}_{0.675}\text{Cr}_{0.075}\text{Si}_{0.25}\text{N}$ a photon energy of 13.0 keV was used [55]. The as-deposited and heat-treated monolayer $\text{Al}_{0.63}\text{Cr}_{0.27}\text{Si}_{0.1}\text{N}$ as well as the heat-treated multilayer were measured with a photon energy of 15.2 keV [56].

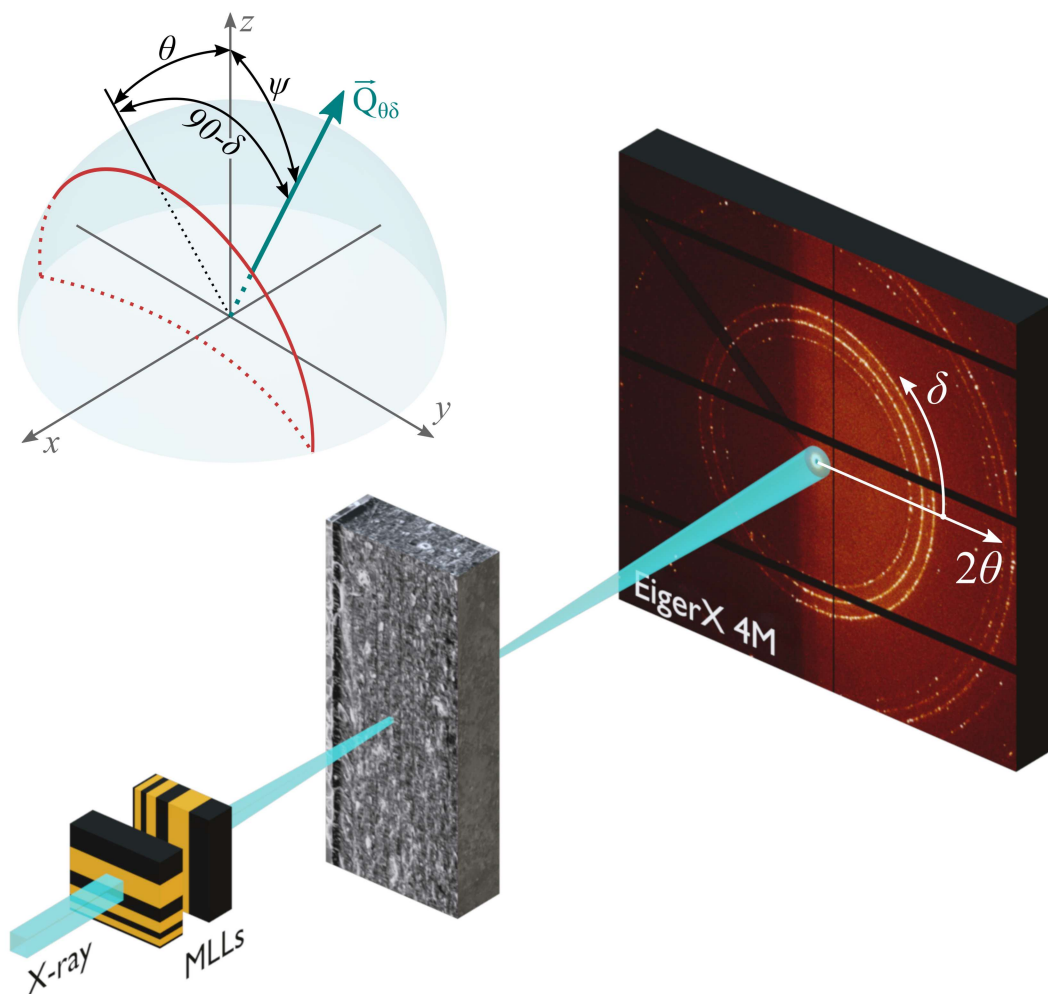


Figure 2.4: CSnanoXRD setup shows the vertically oriented sample that is scanned across in transmissional geometry. The X-ray beam is focussed to a beam size of $\sim 75 \times 75 \text{ nm}^2$ using a pair of multilayer Laue lenses (MLLs). Debye-Scherrer ring with a diffraction angle of 2θ are collected by a 2D detector EigerX 4M.

2.4.3 Phase and texture analysis from collected Debye-Scherrer rings

To extract results from the two-dimensional data, the Debye-Scherrer rings must be integrated azimuthally along δ or radially along θ . With this, the diffracted intensities from all involved diffraction vector orientations are averaged to a one-dimensional dataset. After repeating this integration step for each collected detector image along the cross-sectional scan line, a depth profile of the intensity over 2θ or δ is obtained. Taking into account Eq. 2.1, for a given Bragg angle it is possible to determine the spacing of the lattice planes and thus identify crystalline phases. In principle, the crystalline phases of particular crystal structures are identified by correlating the collected peak positions

with reference powder diffraction files. In a textured material, certain orientations of the crystallites are favoured over others. Thin films are usually characterised by a fibre texture where the fibre axis $\langle hkl \rangle$ is oriented perpendicular to the film-substrate interface. The associated set of lattice planes (hkl) is then parallel to this interface, while the textured crystallites are uniformly oriented around the fibre axis.

Pole figures are commonly used to illustrate crystallographic texture. They depict the stereographic projection of all lattice plane normals in the measured volume with respect to the sample coordinate system. For example, the aforementioned fibre texture is represented by a ring of an equal intensity in a pole figure. By analysing the intensity distribution along the azimuthal direction of a Debye-Scherrer ring, conclusions can be drawn about the texture in the investigated material, *cf.* Fig. 2.5. A relationship between the azimuthal angle δ , Bragg angle θ and polar angle ψ (Fig. 2.4) is given via [48]:

$$\cos \psi = \cos \theta \cos \delta, \quad (2.5)$$

2.4.4 Microstructure analysis from peak broadening

Aside from the peak position, the width of a X-ray diffraction peak can also provide valuable information about the investigated material. A relationship derived by Scherrer correlates the increasing peak widths with the decreasing crystallite sizes [57, 58]:

$$D = \frac{K\lambda}{FWHM \cos \theta}, \quad (2.6)$$

where K is a geometric shape factor depending on the expected crystallite shapes, λ is the X-ray wavelength and θ is the Bragg angle of the peak. The full width at half maximum of the peak is inserted for FWHM in radians. Although D is often referred to as the crystallite size, it actually accounts for domain sizes that coherently scatter the incoming X-rays [57]. It should be noted that peak broadening is influenced by several other factors such as microstrains, dislocations, twin planes, stacking faults, but also the instrumental setup.

2.4.5 Residual stress characterization

In thin films, residual stresses arise as a consequence of the non-equilibrium deposition process and subsequent cooling to room temperature with respective intrinsic stresses, that are ascribed to the coherent epitaxial deposition process, and extrinsic stress contributions, occurring due to a mismatch in thermal expansion coefficients [59, 60]. Therefore, residual stresses can be adjusted by tuning deposition parameters and/or post

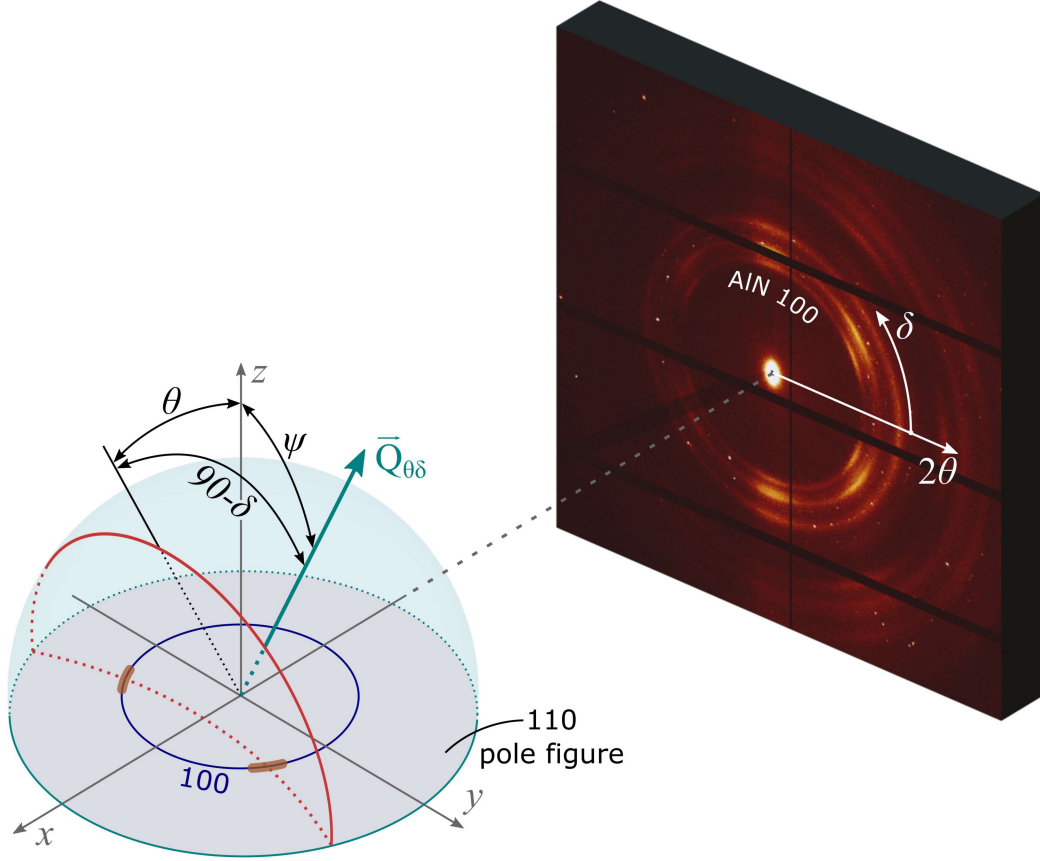


Figure 2.5: The detector image was captured during a cross-sectional line scan through an as-deposited $\text{Al}_{0.63}\text{Cr}_{0.27}\text{Si}_{0.1}\text{N}$ thin film. In a 110 fibre textured thin film the intensity of the 100 Debye-Scherrer ring is increased at the azimuthal angles δ of about 30 and -30 deg.

deposition treatment, such as annealing or shot-peening [59, 61]. Stresses have a significant influence on the mechanical properties of the thin film and therefore need to be properly characterised. In terms of their length scale, type I, II and III residual stresses are distinguished. While type II and III describe residual stresses on the scale of individual crystallites, and can be qualitatively analysed by the peak broadening, type I residual stresses are considered to be the average of stresses in a volume containing a significant number of crystallites [50].

In the context of elastic material properties residual stresses are connected with elastic strains. This allows a characterization of residual stresses from measured lattice spacings d , the theoretical background of which is shortly described in this section. An equibiaxial stress state with $\sigma_{11}(z) \approx \sigma_{22}(z)$, $\sigma_{33}(z) \approx 0$ with negligible shear components $\epsilon_{ij}(z)$, $\sigma_{ij}(z) \approx 0$ is considered. These assumptions are generally valid for thin films

without applied external loads [48, 62].

The elastic strain in a given direction, specified by ϕ and ψ in spherical coordinates, can be expressed by [50, 63]:

$$\epsilon_{\phi\psi} = \epsilon_{11} \cos^2 \phi \sin^2 \psi + \epsilon_{22} \sin^2 \phi \sin^2 \psi + \epsilon_{33} \cos^2 \psi, \quad (2.7)$$

Considering geometrical relation of the CSnanoXRD experiment, *cf.* Fig. 2.4

$$\sin \theta = \cos \phi \sin \psi, \quad (2.8)$$

$$\sin \psi \sin \phi = \cos \theta \sin \delta, \quad (2.9)$$

and abovementioned Eq. 2.7, the strain can be written as a function of the Bragg angle θ and the azimuthal angle δ from the X-ray measurement:

$$\epsilon_{\theta\delta} = \epsilon_{11} \sin^2 \theta + \epsilon_{22} \cos^2 \theta \sin^2 \delta + \epsilon_{33} \cos^2 \theta \cos^2 \delta, \quad (2.10)$$

To introduce stress components, Hooke's law is considered:

$$\epsilon_{ij} = \frac{1 + \nu}{E} \sigma_{ij} - \frac{\nu}{E} \delta_{ij} (\sigma_{11} + \sigma_{22} + \sigma_{33}), \quad (2.11)$$

Further, X-ray elastic constants are introduced to account for the anisotropic elastic properties of the crystallites [50]:

$$-\frac{\nu^{hkl}}{E^{hkl}} \rightarrow S_1^{hkl}, \quad (2.12)$$

$$\frac{1 + \nu^{hkl}}{E^{hkl}} = \frac{1}{2} S_2^{hkl}, \quad (2.13)$$

Finally, the following relationship is obtained for the orientation dependent strain.

$$\epsilon_{\theta\delta}^{hkl}(z) = \frac{d_{\theta\delta}(z) - d_0^{hkl}}{d_0^{hkl}} = \sigma_{11} \left[\frac{1}{2} S_2^{hkl} \sin^2 \theta + S_1^{hkl} \right] + \sigma_{22} \left[\frac{1}{2} S_2^{hkl} \cos^2 \theta \sin^2 \delta + S_1^{hkl} \right], \quad (2.14)$$

A suitable derivation relates the in-plane stress component $\sigma_{22}(z)$ to the ellipticity of the Debye-Scherrer ring, written as a ratio of the measured lattice parameter $d_{\theta\delta}(z)$ and $\sin^2 \delta$ [48, 62].

$$\frac{\partial d_{\theta\delta}(z)}{\partial \sin^2 \delta} = \frac{1}{2} S_2^{hkl} d_0^{hkl} \cos^2 \theta \sigma_{22}(z), \quad (2.15)$$

The unstressed lattice parameter d_0 for a lattice plane hkl as well as the X-ray elastic constant $\frac{1}{2}S_2^{hkl}$ have to be provided for the evaluation and were considered for the evaluated AlN 100 peak as follows:

$$\frac{1}{2}S_2^{hkl} = 0.3903 \cdot 10^{-5} \text{ MPa}^{-1}$$

$$d_0^{100} = 2.69542 \cdot 10^{-1} \text{ \AA}^{-1}$$

2.5 Sample preparation by focused ion beam micromachining

The LEO 1540XB dual-beam FIB workstation was used to prepare thin film cross-sections for a qualitative microstructural analysis in the SEM and to fabricate cantilevers for *in situ* microcantilever bending tests.

2.5.1 Polishing cross-sections-with a focused ion beam

For high-resolution SEM analysis of the thin film cross-sections, a finely polished and defect-free surface is required. Therefore, a protective tungsten layer was first deposited on the thin film surface using the integrated gas injection system (GIS) with an acceleration voltage and deposition current of the Ga^+ ions of 30 kV and 50 pA, respectively. In the next step, the cross-section was cut and polished using decreasing ion currents between 200 pA and 20 pA. Exemplary, Fig. 2.6 shows a FIB-polished cross-section.

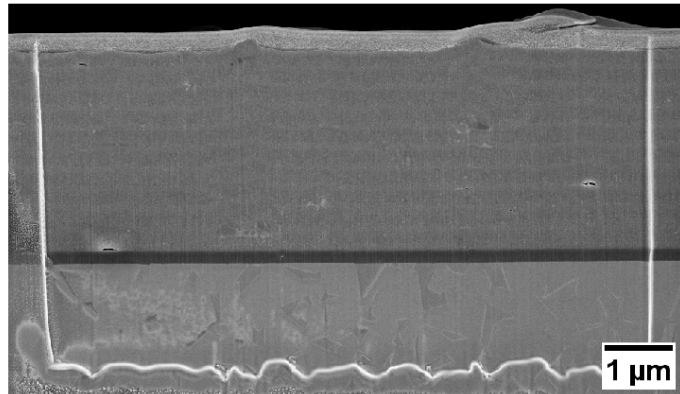


Figure 2.6: Cross-section of the heat-treated multilayer sample polished by a focused ion beam. On top of the polished cross-section a protective deposited tungsten layer of ~ 300 nm is visible as a bright region.

2.5.2 Fabrication of microcantilevers with a focused ion beam

The microcantilevers were fabricated by FIB milling in several steps that can generally be divided into cutting and polishing. The final dimensions of the free-standing microcantilevers are a thickness t of $\sim 3\ \mu\text{m}$, a width B of $\sim 2\ \mu\text{m}$ and a total length of $\sim 15\text{-}20\ \mu\text{m}$, *cf.* Fig. 2.7. In the notched samples, the notch is positioned approximately $2\ \mu\text{m}$ from the base of the cantilever.

In the first step, a small window with dimensions of $\sim 19 \times 6\ \mu\text{m}^2$ was machined using FIB at the thin film surface. A second cut was positioned perpendicular to the long axis of the cantilever in order to define its length. The sample was then rotated 180 deg

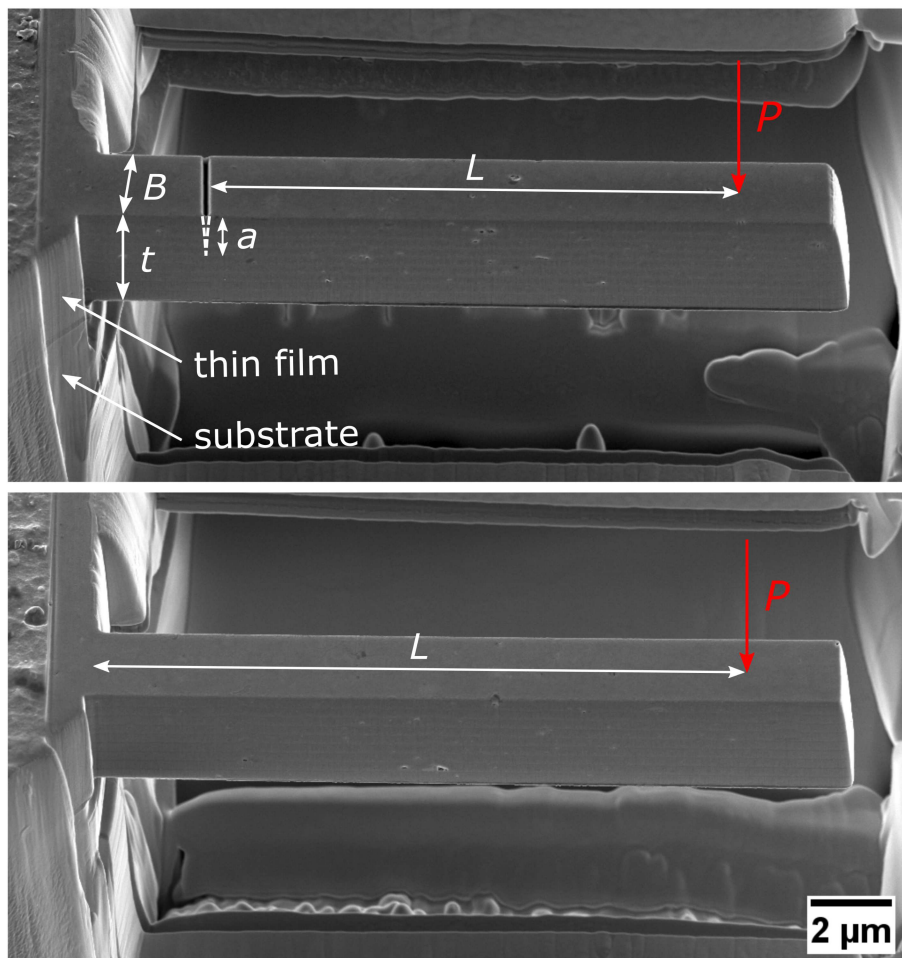


Figure 2.7: Free-standing notched and unnotched microcantilevers are shown in the upper and lower picture, respectively. The geometry of the cantilever is described by the width B and thickness t . In case of the notched cantilever a is the notch depth. Length L corresponds to the testing length in the evaluation process. P indicates the force that is applied by the indenter in the bending tests.

and tilted accordingly to allow machining parallel to the surface to remove the substrate below the cantilever. Beam currents of 2 and 5 nA were used for both steps. With the cantilever in this orientation, a lower current of 500 pA was used to carefully remove the remaining substrate behind the cantilever without removing too much material from the thin film itself. For the final cutting step, the sample was rotated and tilted back to the orientation of the first milling step so that the top and bottom surfaces of the cantilever could be machined with a beam current of 500 pA resulting in an approximately rectangular geometry. After the cutting steps, all sides of the cantilever were polished with a beam current of 100 pA. The order of the polishing steps was front – top – bottom – back of the cantilever. In particular, the back and bottom of the cantilever had to be precisely aligned to ensure the intended stiffness conditions of a cantilever beam. Due to the interaction of the ion beam with the surface to be polished, each face of the cantilever had to be tilted by ~ 1.5 deg from the orientation perpendicular to the ion beam in order to obtain a flat polished surface and a proper rectangular cross-section of the cantilever with dimensions of $t \cong 3 \mu\text{m}$ and $B \cong 2 \mu\text{m}$. A total of eight cantilevers were prepared as described above for each specimen in each condition listed in Table 2.1. In addition, half of the cantilevers were notched for fracture toughness measurements. To do this, a notch with a length slightly less than the width B was cut into the cantilever by FIB, see Fig. 2.7. As a result of milling for approximately 3 min at a current of 5 pA, a sharp notch with thin bridges on the side was obtained. Since the thickness of the cantilever was about $3 \mu\text{m}$, the desired notch depth was 600-800 nm.

2.6 Micromechanical *in situ* bending tests

The FIB-machined notched and unnotched cantilevers were loaded in the out-of-plane direction using a Hysitron PI85 SEM PicoIndenter equipped with a sphero-conical indenter tip as schematically shown in Fig. 2.8. As will be seen later in the results section, the fracture always occurred in the linear elastic regime. The detailed test procedure and evaluation methods are described below.

2.6.1 *in situ* testing in a scanning electron microscope

Microcantilever bending tests were performed in the LEO1540XB dual beam FIB workstation where the loaded cantilever was imaged in the SEM mode. The cantilevers were loaded with a sphero-conical indenter tip with a radius of $0.7 \mu\text{m}$ provided by Synton MDP. In preparation for the tests, the sample with the FIB-machined cantilevers was mounted on a sample holder which was fixed to the piezo stage of the indenter sys-

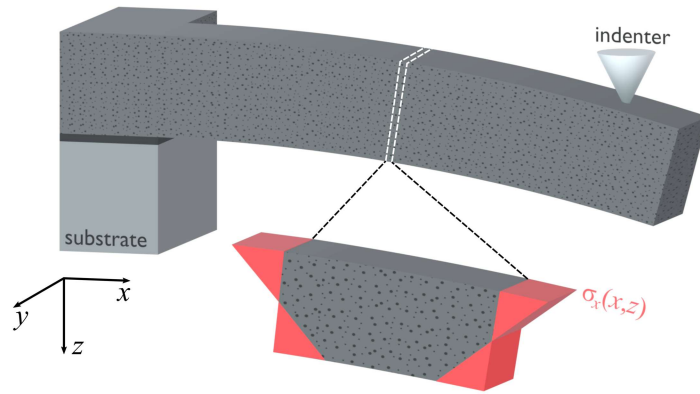


Figure 2.8: A schematic stress distribution across an elastically loaded cantilever.

tem. This was then mounted on the SEM stage and wired to the Hysitron control unit. After achieving a sufficient vacuum, the indenter tip was positioned in the centre of the SEM image using the microscope stage. The indenter tip was then carefully approached by moving the sample with the indenter's piezo stage. As the forward and backward movement of the indenter tip is limited to 5 μm in either direction, the sample must be positioned using only the movement of the piezo stage. To ensure that the cantilever was loaded centrally, the tip first approached the upper edge of the cantilever. Then, after moving the specimen half the width of the cantilever in the negative y direction, the indenter tip was positioned at the level of the cantilever axis and no torsion was induced during the subsequent bending. Once the relative positioning of the cantilever and indenter tip was complete, the test could be started by activating a predefined loading function. In this case, the bending moment was applied at a constant loading rate of 20 nm/s until failure occurred.

Load-displacement data was recorded by the Hysitron control unit. The test length, *i.e.* the distance between the indenter and the fracture initiation point, was determined from an SEM image after the test. Other necessary geometric data were determined by SEM imaging prior to the *in situ* testing, while the actual notch depths of the cantilevers (intended for fracture toughness testing) were evaluated *ex situ* after fracture. Figures 2.9a, b, and c show a representative cantilever before, during and after the bending test, respectively. It should be noted that during the recording of the bending test, the dwell time of the electron beam was reduced in order to capture the movement of the indenter and cantilever, hence the image quality is lower.

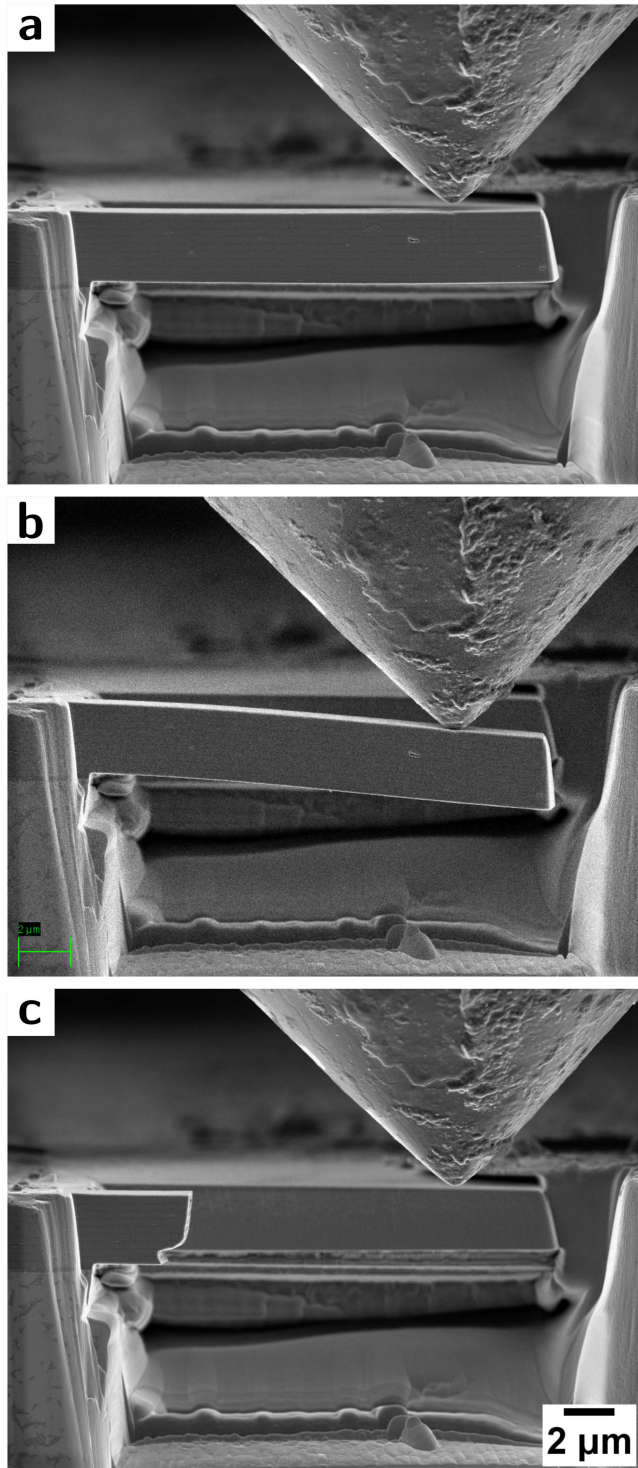


Figure 2.9: A representative cantilever of an as-deposited multilayer sample before (a), during (b) and after the bending test (c).

2.6.2 Evaluation of Young's modulus

Four cantilevers of each thin film type (*cf.* Table 2.1) remained unnotched in order to determine Young's Modulus E as well as the fracture stress σ_f . A formula for the Young's Modulus can be derived from the differential equation for a deflected beam [64]:

$$EI_y \frac{d^2w}{dx^2} = -M_y = -P(x - L), \quad (2.16)$$

where $I_y = Bt^3/12$ is the second moment of inertia for bending around the y -axis, w is the deflection of the beam in the z -direction. M_y is the applied bending moment around the y -axis and is formed by the applied force P acting at distance L . This formula can be applied in the case of a linear elastic material behaviour, where the displacements and the angle of rotation must be small, *i.e.* the cantilever can be treated as a long beam [64]. It can be demonstrated that these requirements are met by showing that the complementary energy due to the lateral force is much smaller than the complementary energy due to the bending moment M_y , these requirements are fulfilled for the underlying cantilever geometries [64].

After two integrations, the following expression is obtained, where C_1 and C_2 are integration constants:

$$EI_y w(x) = -\frac{Px^3}{6} + \frac{PLx^2}{2} + C_1x + C_2, \quad (2.17)$$

Assuming that both the displacement and the slope of the bending curve at the base of the cantilever are zero, *i.e.* the cantilever base is infinitely stiff, the following formula is obtained.

$$w(x=0) = 0, \quad \frac{dw(x=0)}{dx} = 0, \quad (2.18)$$

$$EI_y w(x) = -\frac{Px^3}{6} + \frac{PLx^2}{2}, \quad (2.19)$$

Applying these conditions and transforming the expression for $x = L$ and taking into account the second moment of inertia for a rectangular cross-section, a formula for Young's modulus is obtained as follows.

$$E = \frac{4P}{Bw} \left(\frac{L}{t} \right)^3, \quad (2.20)$$

Obviously, Young's modulus depends linearly on the ratio of force to displacement, see Eq. 2.20. For this reason, the slope of the load-displacement curve is used in the

formula to make the evaluation more convenient.

$$E = \frac{4\Delta P}{B\Delta w} \left(\frac{L}{t}\right)^3, \quad (2.21)$$

In addition, the system compliance has previously been empirically determined to be $0.17 \text{ nm}/\mu\text{N}$ [46]. Inverting the measured slope of the load-displacement curve gives the total measured compliance. This has to be corrected by subtracting the system compliance. This step preserves the compliance of the cantilever and allows a correct determination of the Young's modulus of the cantilever, eliminating the influence of the experimental setup.

$$E = \frac{4}{B} \left(\frac{\Delta w}{\Delta P} - 0.17 \frac{\text{nm}}{\mu\text{N}}\right)^{-1} \left(\frac{L}{t}\right)^3, \quad (2.22)$$

2.6.3 Fracture stress evaluation

The fracture stress σ_f for a bending experiment describes the maximum tensile stress at which the cantilever fails. An expression for this can be easily derived by considering the bending formula for a beam geometry assuming linear elastic material behaviour [64].

$$\sigma_x(x, z) = \frac{M_y(x)}{I_y} z, \quad (2.23)$$

Herein, z is the distance from the neutral axis of the loaded beam, M_y is the bending moment that deflects the beam and I_y is the moment of inertia of the cantilever cross-section. The maximum distance from the neutral fibre in a cantilever is half its thickness t , so $z = t/2$. The maximum bending moment, measured exactly at the moment of fracture, results from the force P_{max} applied at distance $x = L$. The maximum tensile stress is obviously measured at the restraint of the cantilever on the face where the force is applied in this case.

$$\sigma_f = \frac{6P_{max}L}{Bt^2}, \quad (2.24)$$

2.6.4 Fracture toughness evaluation

The previous two sections described evaluation methods for unnotched cantilevers and derived expressions for Young's modulus and fracture stress. In contrast, for notched cantilevers the fracture toughness K_{Ic} can be determined as described in Ref. [65].

$$K_{Ic} = Y \left(\frac{a}{t}\right) \sigma_f \sqrt{\pi a}, \quad (2.25)$$

For this evaluation to be valid, the following geometric conditions must be met [66]:

$$a, t - a, B \geq 2.5 \left(\frac{K_{Ic}}{\sigma_f} \right)^2, \quad (2.26)$$

In addition to the fracture stress σ_f and the notch depth a , also a dimensionless geometry factor Y is required to calculate K_{Ic} . As indicated in Eq. 2.25, this factor depends only on the notch depth a and the cantilever thickness t and is expressed as follows [65]:

$$Y \left(\frac{a}{t} \right) = \sqrt{\frac{2t}{\pi a} \tan \left(\frac{\pi a}{2t} \right)} \frac{0.923 + 0.199 (1 - \sin \left(\frac{\pi a}{2t} \right))^4}{\cos \left(\frac{\pi a}{2t} \right)}, \quad (2.27)$$

In linear elastic fracture mechanics, the plastic zone in front of the propagating crack is expected to be small compared to the region determined by the stress intensity factor K_I [66]. An analysis by Irwin allows the size of this plastic zone r_p , also known as the process zone, to be calculated. Furthermore, Irwin proposed a refinement of the fracture toughness evaluation by taking into account an effective crack length a_{eff} [66]:

$$r_p = \frac{1}{2\pi} \left(\frac{K_{Ic}}{\sigma_f} \right)^2, \quad (2.28)$$

$$a_{eff} = a + r_p, \quad (2.29)$$

This correction of the crack length is valid if the size of the plastic zone is less than two percent of the notch depth, width and thickness of the cantilever [66]. After correcting Eq. 2.25 for the effective crack length and inserting Eq. 2.24 for σ_f , the following expression is obtained for K_{Ic} :

$$K_{Ic} = \frac{6P_{max}L}{Bt^2} \sqrt{\frac{2t}{\pi a_{eff}} \tan \left(\frac{\pi a_{eff}}{2t} \right)} \frac{0.923 + 0.199 (1 - \sin \left(\frac{\pi a_{eff}}{2t} \right))^4}{\cos \left(\frac{\pi a_{eff}}{2t} \right)}, \quad (2.30)$$

2.6.5 Analytical solution for the determination of crack lengths

A closer examination of the force-displacement curves of a conducted bending experiment provides more information about the material response. Drops in the applied force mostly represent localized fracture events such as the failure of the notch bridges [65]. If the load drop is additionally accompanied by a significant change in cantilever stiffness, this indicates stable or stepwise crack propagation as opposed to catastrophic failure at the final fracture event. Alfreider *et al.* have derived an analytical solution for the determination of crack lengths by relating a change in cantilever stiffness to a change in

crack length [67]. A schematic of the geometry used for analysis is given in Fig. 2.10, while mathematical derivation based on findings from [68, 69] leads to the following relation:

$$\int_0^a \frac{a}{t} Y \left(\frac{a}{t} \right)^2 da = \frac{\left(\frac{k_0}{k} - 1 \right) L}{18\pi (1 - \nu^2) r^2}, \quad (2.31)$$

Here k_0 and k are the stiffnesses of the unnotched and notched beam, respectively and ν is Poisson's ratio. While a , t and L are geometrical parameters of the cantilever already described in the previous sections, r is defined as the ratio $(L - x_c)/L$, where x_c is the distance of the crack from the base.

In this work, the load-displacement curves obtained from bending experiments performed on the heat-treated multilayer specimen exhibited stepwise crack propagation. For this reason, an analytical evaluation was carried out on each of the notched specimens, where a Poisson's ratio of $\nu = 0.25$ was assumed for all specimens. In parallel, SEM analysis of the fracture surfaces was performed to validate the analytical results.

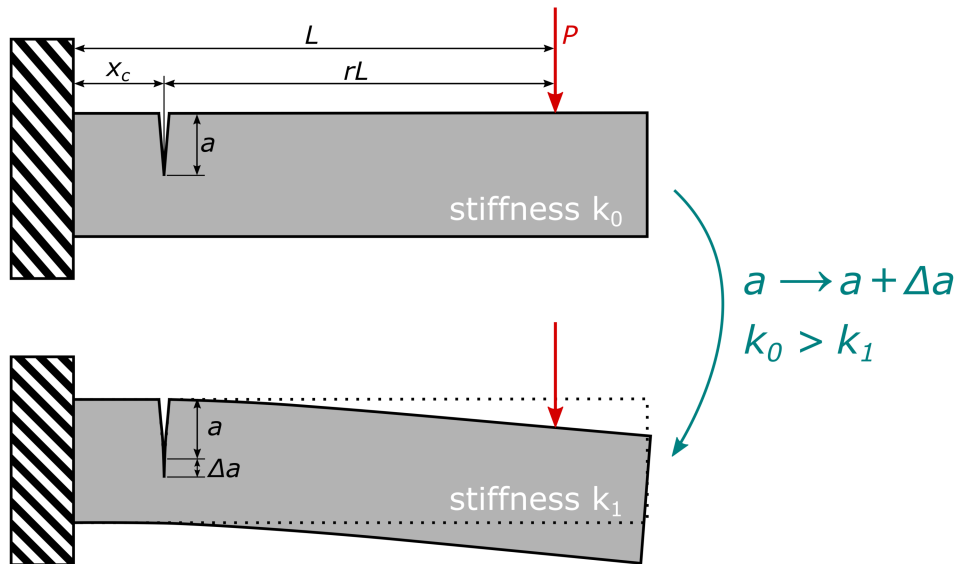


Figure 2.10: Upon crack propagation in a cantilever its stiffness is reduced. This allows for the analytical evaluation of crack lengths from the measured load-displacement curves.

3

Results

3.1 SEM Analysis of thin film morphology and microstructure

The first step in the experimental work was to examine the microstructure of the deposited thin films by SEM. As designated by the deposition conditions, the sublayer thicknesses of the multilayered thin film are ~ 250 and ~ 50 nm for the sublayers having lower and higher Si content, respectively (Fig. 3.1b). Also the TiN bonding layer with a thickness of ~ 250 nm is visible for the multilayer and $\text{Al}_{0.675}\text{Cr}_{0.075}\text{Si}_{0.25}\text{N}$ films in Figs. 3.1b and f. The cross-sections are characterised by a glassy and featureless morphology, no columnar grain structure can be identified. This confirms the formation of a nanocomposite microstructure due to sufficient addition of Si [34, 70]. The morphology remains glassy and featureless after the applied heat-treatment. However, the micrograph of the heat-treated multilayer clearly shows a microstructural modification due to the formation of precipitates, *cf.* Fig. 3.1e.

FIB polished cross-sections allowed a qualitative microstructural analysis at higher magnifications. All analysed samples show the incorporation of droplets resulting from the arc evaporation process and disturbing the uniform film growth [13], *cf.* Fig. 3.2. They are typically non-uniform in shape and size and can be either amorphous or crystalline [71]. Micrographs (a)-(e) in Fig. 3.2 reveal a layered substructure with a periodicity of about 30 nm for all investigated thin film systems. This is typical of thin films grown by periodically rotating in and out of a line of sight deposition process [72].

As shown in Figs. 3.2a and d, the heat-treatment of the reference layer with the lower Si content ($\text{Al}_{0.63}\text{Cr}_{0.27}\text{Si}_{0.1}\text{N}$) leads to the formation of globular precipitates which are mainly located at the boundaries of the previously mentioned deposition-induced substructure. The reference sublayer with the higher Si content ($\text{Al}_{0.675}\text{Cr}_{0.075}\text{Si}_{0.25}\text{N}$) remains unaffected in terms of precipitation formation at least at the resolution of the SEM Figs. 3.2c and f. Slight redistribution of concentration variations is indicated by Fig. 3.2f, where the deposition-induced periodic substructure is diminished after the heat-treatment. After the applied heat-treatment, precipitates are observed in the thicker sublayers of the multilayer sample thin film as shown in Fig. 3.2e. In contrast,

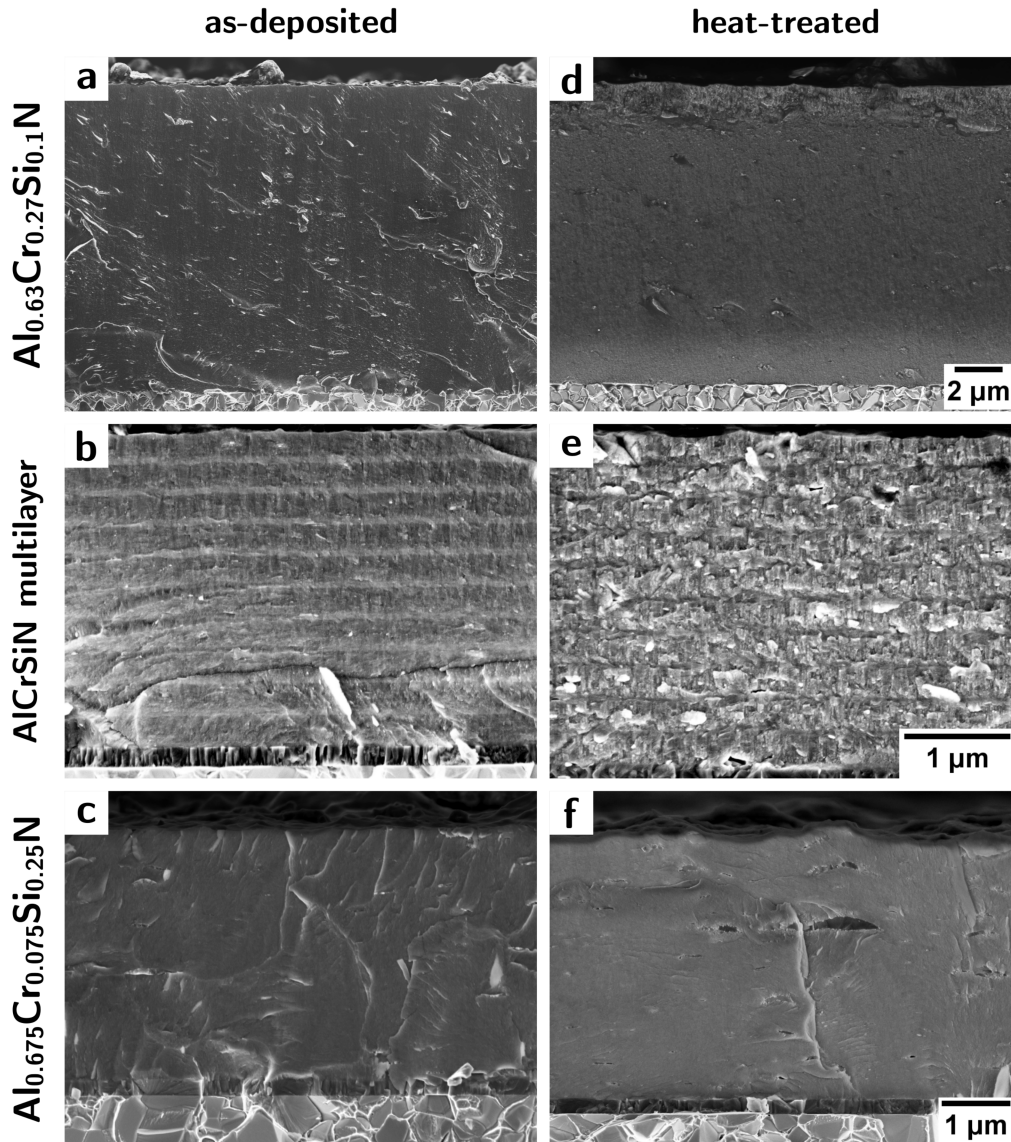


Figure 3.1: SEM micrographs imaging of fracture cross-sections of the two reference thin films and the multilayer in the as-deposited (a, b, c) as well as heat-treated state (d, e, f). Please note that for (a) and (d), (b) and (e) as well as for (c) and (f) the same scale bar applies, respectively.

the thinner sublayers do not show any precipitates. This observation is as expected since the multilayer was deposited with the same parameters alternating the $\text{Al}_{0.63}\text{Cr}_{0.27}\text{Si}_{0.1}\text{N}$ and $\text{Al}_{0.675}\text{Cr}_{0.075}\text{Si}_{0.25}\text{N}$ materials. More detailed results regarding the morphology and chemical composition of the annealed nanocomposite microstructure will follow in the next section of TEM analysis.

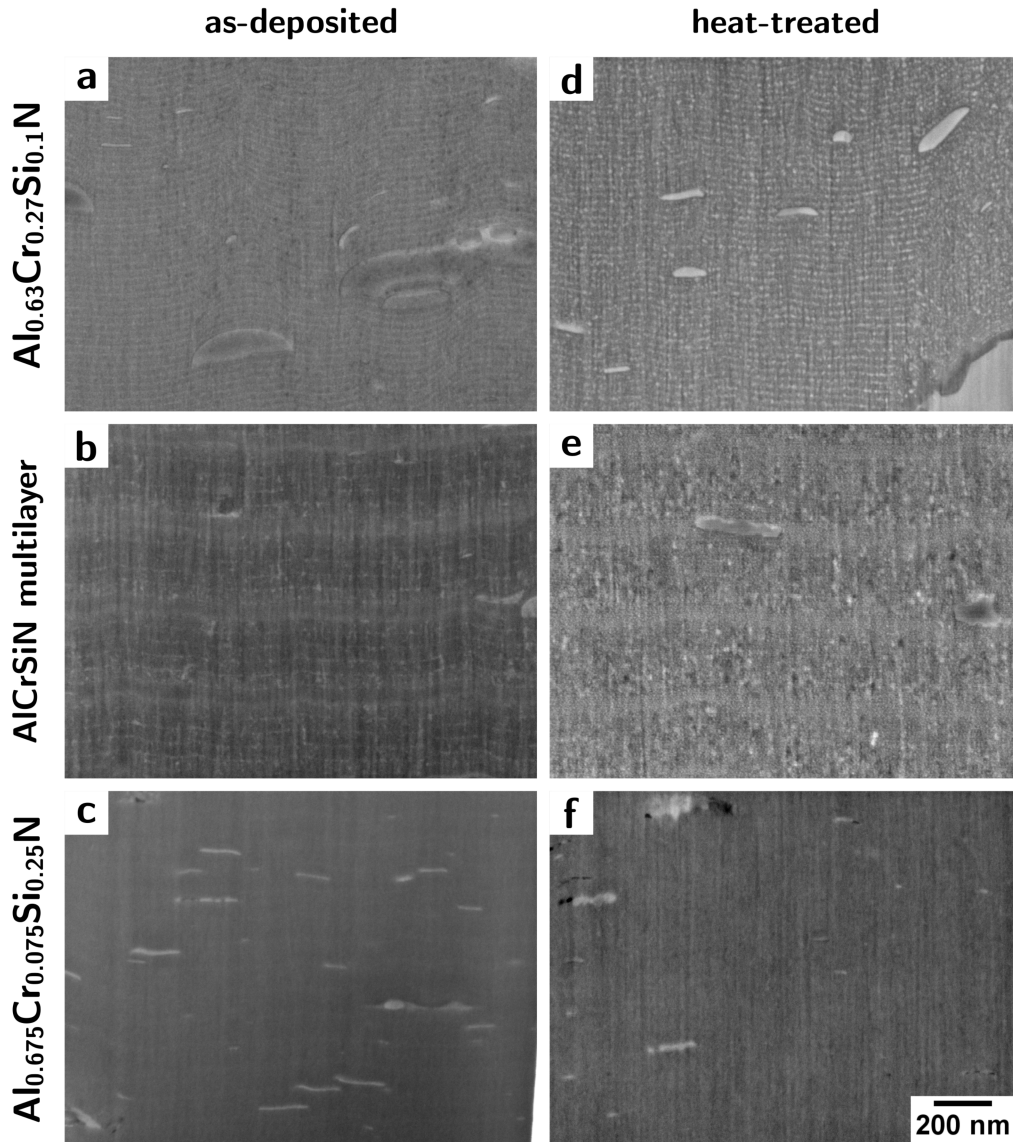


Figure 3.2: SEM images of FIB-polished cross-sections of the two reference thin films and the multilayer in the as-deposited (a, b, c) as well as heat-treated state (d, e, f). The scalebar applies to all images.

3.2 TEM characterization of microstructure and chemical properties

In this chapter the results of EDS performed in TEM are presented first for the two reference thin films and then for the multilayer. TEM characterization was carried out for the heat-treated samples.

3.2.1 $\text{Al}_{0.63}\text{Cr}_{0.27}\text{Si}_{0.1}\text{N}$ monolithic thin film

As described in the previous section, SEM analysis revealed the presence of a layered microstructure with a periodicity of around 30 nm for both the as-deposited and annealed specimens, *cf.* Figs. 3.2a and d. For the $\text{Al}_{0.63}\text{Cr}_{0.27}\text{Si}_{0.1}\text{N}$ thin film, this was confirmed by TEM analysis, *cf.* high-angle annular dark-field (HAADF) micrograph in Fig. 3.3a. Furthermore, EDS data show that Cr is enriched at the boundaries of these sublayers, see in particular the respective elemental distribution presented in Fig. 3.3b obtained from a cut through the colour maps in (a).

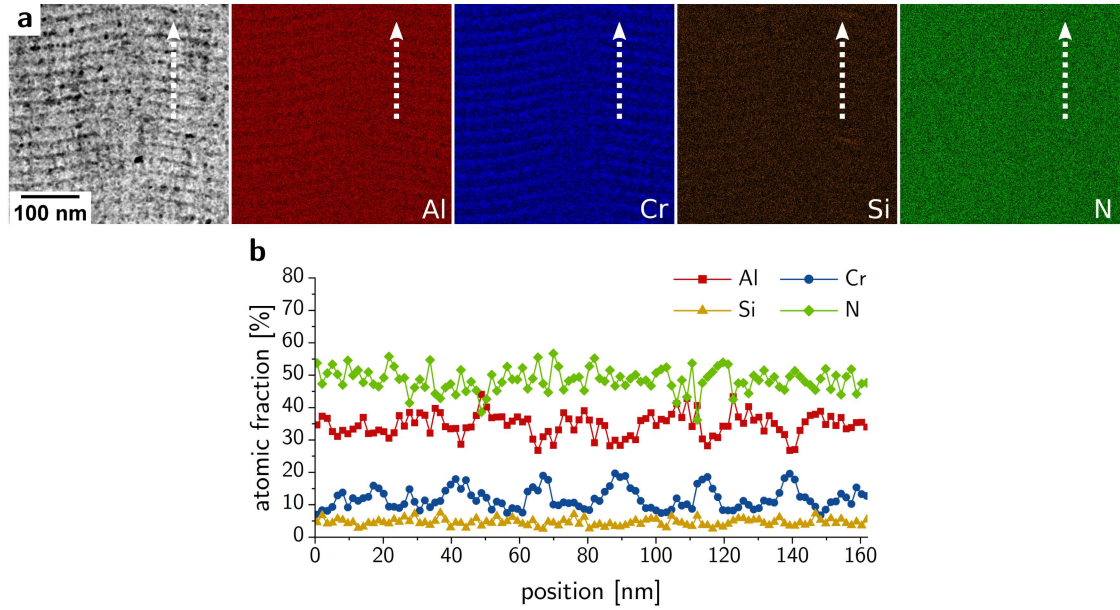


Figure 3.3: HAADF micrograph and elemental colour maps obtained by EDS mapping in TEM for the heat-treated $\text{Al}_{0.63}\text{Cr}_{0.27}\text{Si}_{0.1}\text{N}$ thin film in (a). The graph presented in (b) shows the elemental composition along the line that is oriented parallel to the film growth direction.

At the substructure boundaries the Cr content increases up to 20 at.%, while in the centre of these sublayers it decreases to ~ 10 at.%. In general, the atomic fractions revealed by the line scan correspond approximately to the expected composition of the cathodes used for deposition of the $\text{Al}_{0.63}\text{Cr}_{0.27}\text{Si}_{0.1}\text{N}$ monolayer. The average Al content is around 35 at.%, while the Cr content is at around 15 at.%. Si and N content are ~ 5 and ~ 50 at.%, respectively, indicating a thin film slightly enhanced in the heavier Cr, as found in literature [34].

3.2.2 $\text{Al}_{0.675}\text{Cr}_{0.075}\text{Si}_{0.25}\text{N}$ monolithic thin film

In contrast to the $\text{Al}_{0.63}\text{Cr}_{0.27}\text{Si}_{0.1}\text{N}$ thin film, $\text{Al}_{0.675}\text{Cr}_{0.075}\text{Si}_{0.25}\text{N}$ appears more uniform after the heat-treatment. A periodic element variation can be excluded by looking at the EDS results in Fig. 3.4. Two line scans perpendicular (Fig. 3.4b) and parallel (Fig. 3.4c) to the film growth direction confirm that the chemical composition is constant throughout the thin film. The thin films composition is in good agreement with the cathode composition given in Table 2.1, the line scans in Fig. 3.4b and c show ~ 34 at.% Al and ~ 3 at.% Cr, while Si and N are at ~ 12 and ~ 50 at.%, respectively.

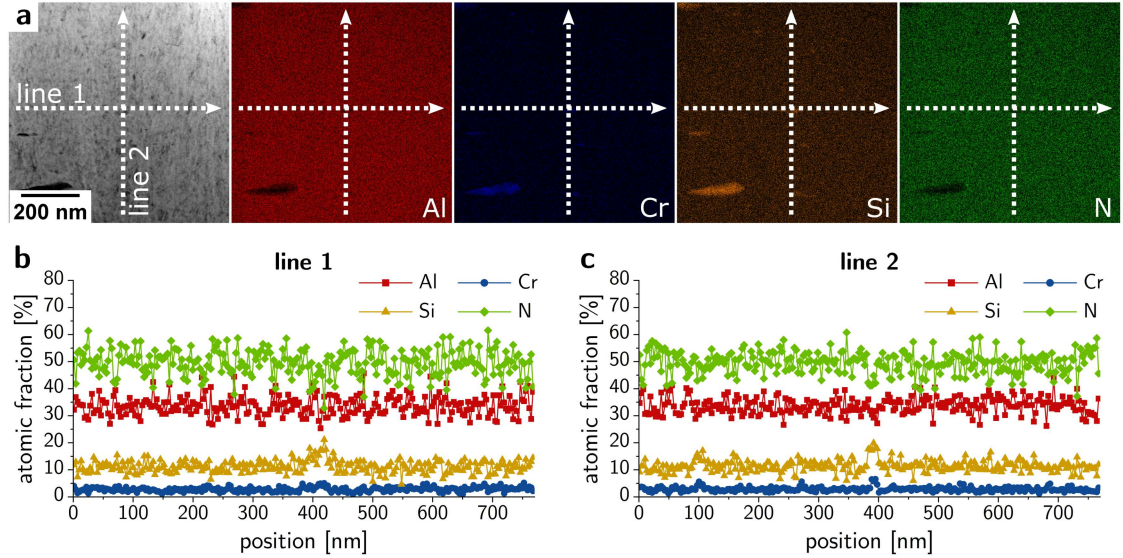


Figure 3.4: HAADF micrograph and elemental colour maps obtained by EDS mapping in TEM for the heat-treated $\text{Al}_{0.675}\text{Cr}_{0.075}\text{Si}_{0.25}\text{N}$ thin film are presented in (a). The elemental composition profiles along the lines 1 and 2, that are oriented perpendicular and parallel to the growth direction of the thin film, are presented in (b) and (c), respectively.

3.2.3 AlCrSiN multilayer thin film

The periodic sequence of the two alternating elemental compositions in the multilayer is nicely shown in Fig. 3.5. Correlating the analysis of the thicker layers with the results of $\text{Al}_{0.63}\text{Cr}_{0.27}\text{Si}_{0.1}\text{N}$, *cf.* Sec. 3.2.1, the Al content increases while the Cr content decreases in the multilayer sample as shown in Fig. 3.5b. The Cr content varies periodically in the thicker layers and remains constant in the thinner layers, corresponding to the data from the $\text{Al}_{0.63}\text{Cr}_{0.27}\text{Si}_{0.1}\text{N}$ film in Fig. 3.3 and from the $\text{Al}_{0.675}\text{Cr}_{0.075}\text{Si}_{0.25}\text{N}$ film in Fig. 3.4.

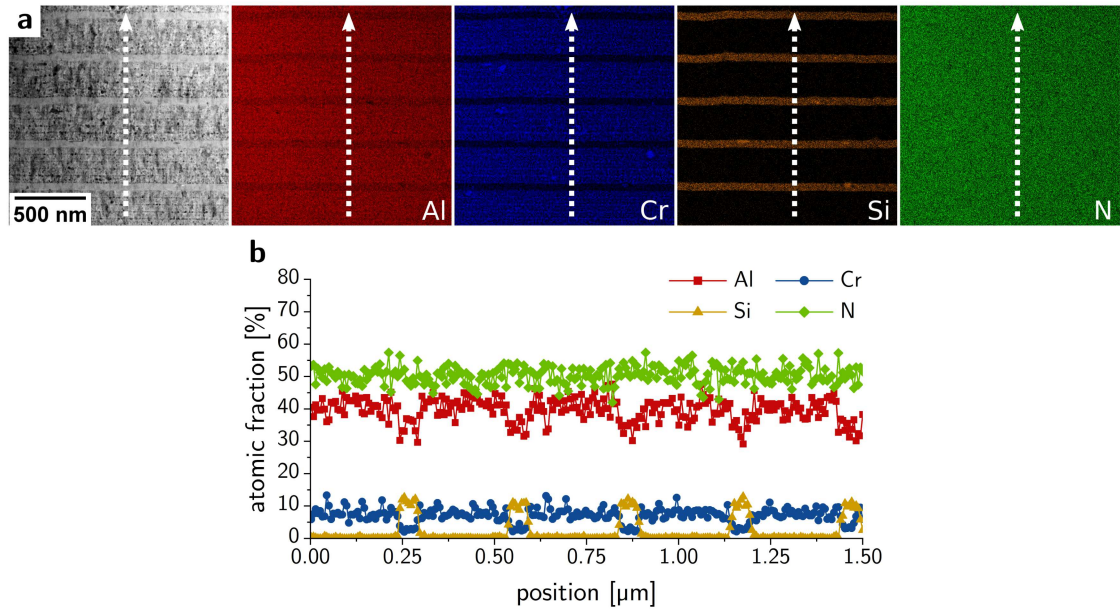


Figure 3.5: HAADF micrograph and elemental colour maps obtained by EDS mapping in TEM for the heat-treated multilayer are presented in (a). The graph in (b) shows the elemental composition along the line oriented parallel to the growth direction of the thin film.

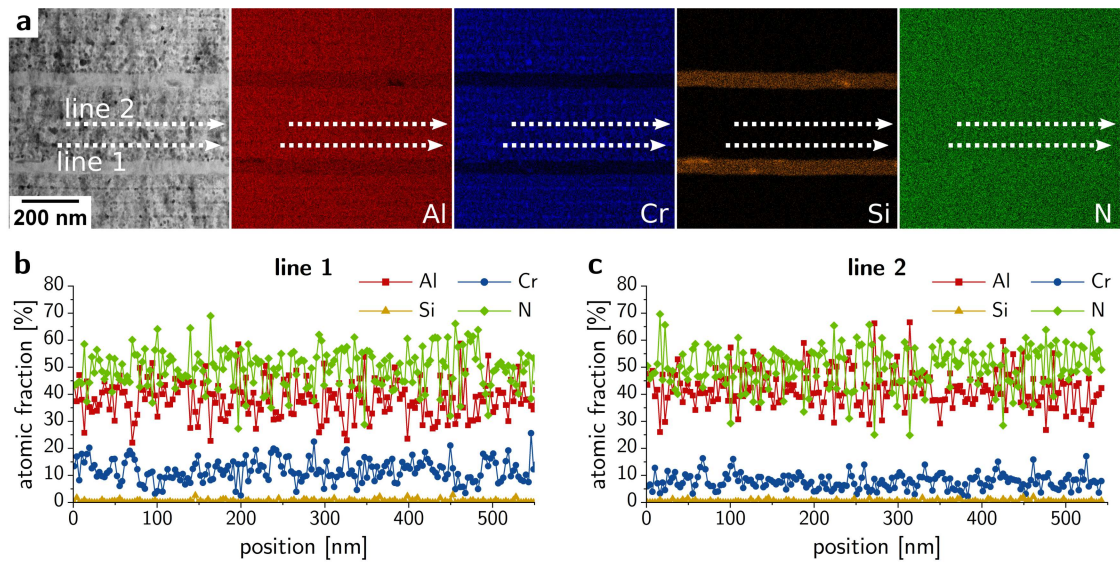


Figure 3.6: HAADF micrograph and elemental colour maps for the multilayer received by EDS mapping conducted in TEM. The two graphs in (b) and (c) show the atomic contents along the respective lines in the micrograph (a).

As previously described, the boundaries of the layered substructure in the thicker sublayers are favoured by Cr, with globular precipitates forming preferentially at these

locations. This is corroborated by the composition along line 1 in Fig. 3.6b is exactly at the boundary of the periodic substructure and indicates an increased Cr content. In contrast, line 2 in Fig. 3.6c is in the middle of an approximately 30 nm thick layer of this substructure and displays a significantly lower Cr content compared to line 1.

Finally, an EDS analysis of a globular precipitate is shown in Fig. 3.7. In the centre of the precipitate the Cr content increases while Al decreases to the same content of ~25 at.% as shown in Fig. 3.7b. The composition of the precipitate strongly indicates the formation of a Cr-rich cubic Cr(Al)N phase.

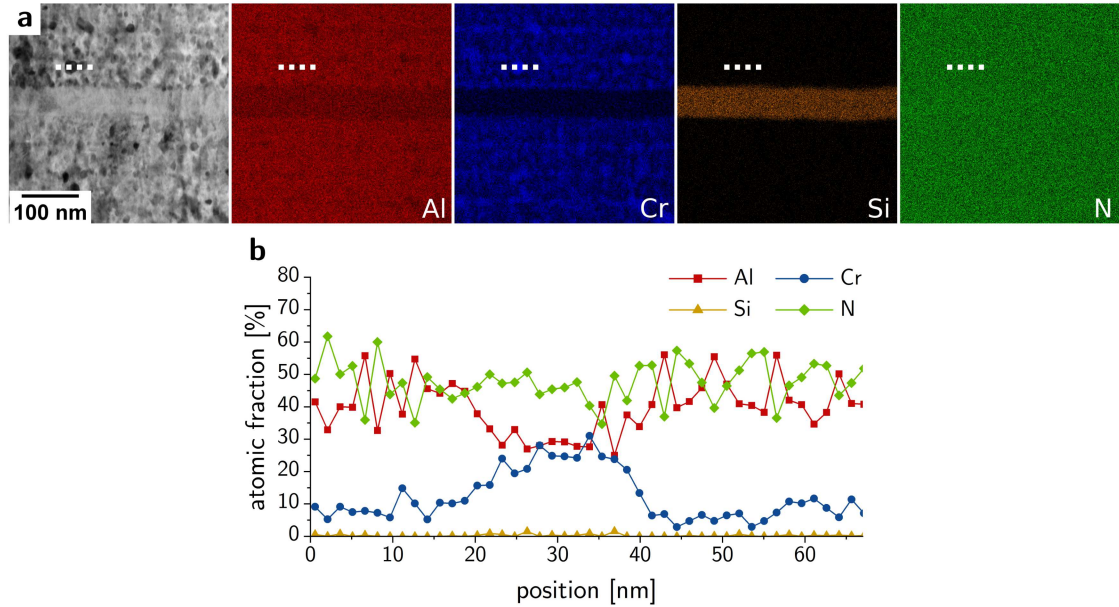


Figure 3.7: HAADF micrograph and elemental colour obtained by EDS mapping in TEM for the heat-treated multilayer. The line shown in the TEM micrograph (a) was set to display the elemental composition across a precipitate in (b).

3.3 Cross-sectional X-ray nanodiffraction measurements

The next step of characterizing the thin films on a nanoscale was to evaluate the crystal-line phases, texture, microstructure and residual stress, as described in Sec. 2.4. Please note for the phase plots that the synchrotron measurements were carried out at different beamtimes where different photon energies were used, *cf.* Sec. 2.4.2. However, this still enables a correlative comparison of the phase plots as only the peak positions are shifted.

3.3.1 $\text{Al}_{0.63}\text{Cr}_{0.27}\text{Si}_{0.1}\text{N}$ monolithic thin film

The phase plots in Figs. 3.8 and 3.9 display wurtzite AlN 100 and 101 as well as cubic CrN 111 and 200 peaks. This confirms the prediction of a dual-phase Si-containing nanocomposite structure with wurtzite Al(Cr)N and cubic Cr(Al)N in the as-deposited and heat-treated thin films. However, the CrN 200 peak is more pronounced after the heat-treatment, *cf.* Figs. 3.8 and 3.9. Following the results from TEM analysis in Sec. 3.2.1 this approves the formation of cubic Cr(Al)N precipitates as a result of the annealing. The TiN 111 and 200 reflections range up to a thickness of approximately 250 nm and can therefore be clearly correlated with the deposited TiN bonding layer. As the thin films were deposited on tungsten carbide substrates, WC 001 and 101 peaks are observed immediately in the vicinity of the interface between substrate and bonding layer.

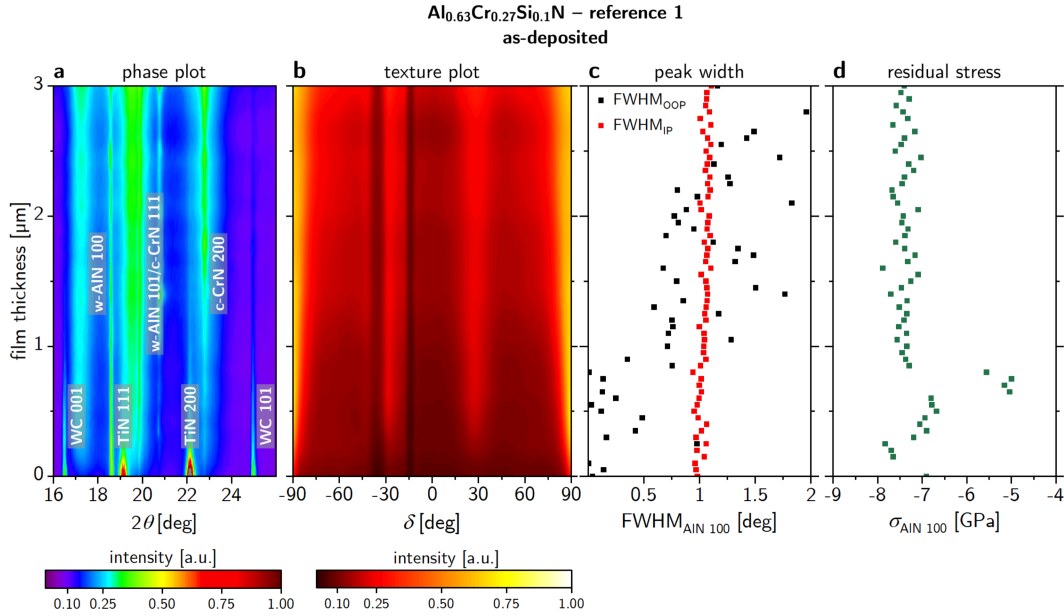


Figure 3.8: CSnanoXRD data retrieved from the as-deposited $\text{Al}_{0.63}\text{Cr}_{0.27}\text{Si}_{0.1}\text{N}$ film. In (a) the phase plot obtained by an azimuthal integration of the corresponding Debye-Scherrer rings is shown, while in (b) the azimuthal distribution of the diffracted intensities indicates a $\langle 110 \rangle$ fibre texture. From the cross-sectional variation in the FWHM of the AlN 100 peak a crystallite size of ~ 5 nm was calculated (c). The residual stress evaluated from the AlN 100 Debye-Scherrer ring shows an oscillatory variation around a mean value of ~ -7 GPa (d).

Azimuthal intensity distributions of the AlN 100 Debye-Scherrer ring were plotted to investigate texture in the thin film. In both as-deposited and heat-treated thin films, azimuthal intensity maxima were observed slightly below 30 deg and just above -30 deg.

With Eq. 2.5 a polar angle ψ of 28.8 deg is calculated between the 110 and 100 AlN lattice planes for 2ψ amounting to 17.4 deg. Hence, the evaluated data indicates a $\langle 110 \rangle$ fibre texture where the $\{110\}$ planes are oriented approximately perpendicular to the growth direction of the thin film [13, 34]. A comparison of the respective texture plots in Figs. 3.8b and 3.9b shows that heat-treatment leads to a slightly more pronounced fibre texture.

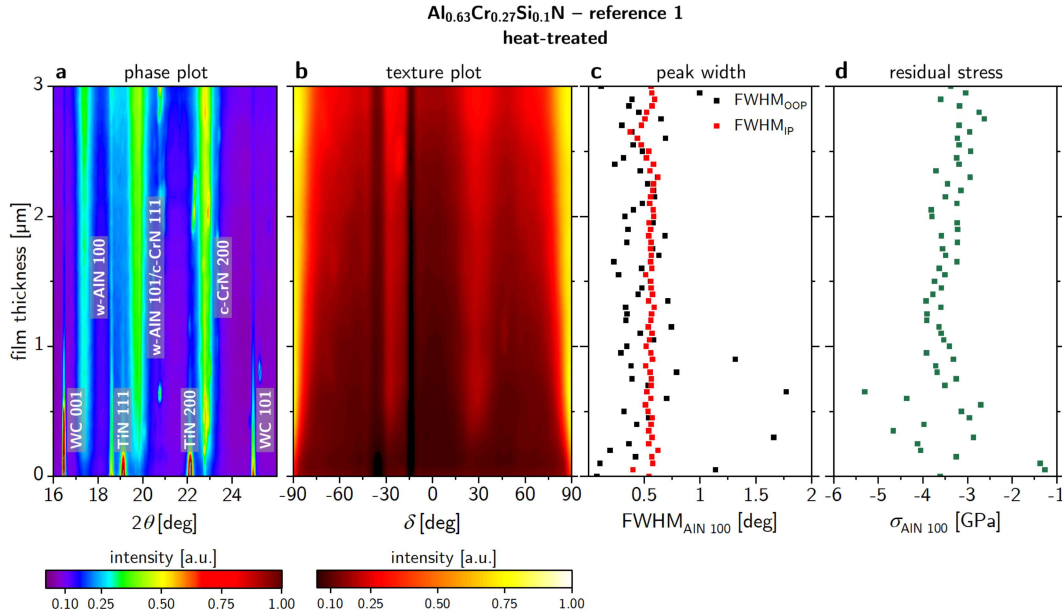


Figure 3.9: CSnanoXRD data retrieved from the heat-treated $\text{Al}_{0.63}\text{Cr}_{0.27}\text{Si}_{0.1}\text{N}$ film. In (a) the phase plot obtained by an azimuthal integration of the corresponding Debye-Scherrer rings is shown, while in (b) the azimuthal distribution of the diffracted intensities indicates $\langle 110 \rangle$ fibre texture. The cross-sectional FWHM variation of the AlN 100 peak is decreased with respect to the as-deposited thin film due to temperature-activated microstructural recovery processes (c). The residual stress evaluated from the AlN 100 Debye-Scherrer ring shows a variation around a mean value of ~ 3.5 GPa (d).

Peak broadening of the AlN 100 peak was analysed approximately for the out-of-plane (OOP) and in-plane (IP) orientation of the diffraction vector, namely at the azimuthal angles δ of -90 deg and 0 deg, respectively. In the as-deposited sample, FWHM for the in-plane orientation marginally increases in the growth direction, *cf.* Fig. 3.8c. Applying the Scherrer formula for a FWHM value of 1 deg a crystallite size of ~ 5 nm is computed, confirming the presence of nanosized crystallites. In contrast, FWHM for the out-of-plane orientation in the as-deposited sample is non-uniform and largely scatters in the growth direction. It seems as the FWHM shows a decreasing trend as the substrate is approached, however, the large variations between the datapoints disallow

a clear correlation to a changing crystallite size. The scattering of the FWHM data is mainly caused by the relatively low intensity of the particular diffraction peaks. Heat-treatment led to a decrease in peak widths for both out-of-plane and in-plane orientation, *cf.* Fig. 3.9c. FWHM for both orientations amounts to ~ 0.5 deg, which accounts to a size of coherently diffracting domains of ~ 10 nm. Also, the variation in the out-of-plane FWHM is lowered. The reduced peak broadening is attributed to temperature-activated microstructural recovery and grain growth processes of the embedded crystallites in the nanocomposite structure [34].

For the depth-resolved residual stress analysis the position of the AlN 100 peaks was analysed. In the evaluation procedure the respective peaks were fitted at 36 different azimuthal angles δ uniformly distributed along the Debye-Scherrer ring. Applying this fitting procedure to all detector images captured along the cross-sectional scan, a depth-profile of the residual stresses was obtained. In the as-deposited state of $\text{Al}_{0.63}\text{Cr}_{0.27}\text{Si}_{0.1}\text{N}$ compressive residual stresses of about -7 GPa were revealed. Microstructure recovery induced by the heat-treatment [73] led to a reduction in the amount of compressive residual stresses to about -3.5 GPa, *cf.* Figs. 3.8d and 3.9d [34].

3.3.2 $\text{Al}_{0.675}\text{Cr}_{0.075}\text{Si}_{0.25}\text{N}$ monolithic thin film

Phase analysis of the second reference thin film revealed wurtzite AlN, strong AlN 100 and 101 peaks are observed for both as-deposited and heat-treated samples, *cf.* Figs. 3.10a and 3.11a. Cubic CrN could not be clearly identified in the as-deposited sample as the CrN 200 peak at 26.6 deg is not present in the phase plot and the possible CrN 111 peak overlaps with the measured AlN 101 peak at a 2θ of ~ 23 deg as shown in Fig. 3.10a. Apart from that, in comparison with $\text{Al}_{0.63}\text{Cr}_{0.27}\text{Si}_{0.1}\text{N}$ the Al/Cr ratio is higher in the $\text{Al}_{0.675}\text{Cr}_{0.075}\text{Si}_{0.25}\text{N}$ thin film, where pure wurtzite crystalline phase formation is expected [28–30]. As a result, a formation of wurtzite Al(Cr)N is preferred over the formation of cubic Cr(Al)N phases in the nanocomposite structure. After the heat-treatment no significant change of the intensities of the AlN and CrN peaks could be observed in the phase plot as shown in Figs. 3.10a and 3.11a. This is due to the increased Si content and higher Al/Cr ratio diminishing the formation of cubic CrN phase, as seen in literature [34], and apparently suppressing precipitation of c-Cr(Al)N, which is in agreement with the TEM results presented in Sec. 3.2.2. The TiN 111 and 200 peaks were measured in the as-deposited (Fig. 3.10a) and annealed sample (Fig. 3.11a) and are attributed to the bonding layer. In both conditions the WC 100 peak relates to the substrate material of the deposited thin films.

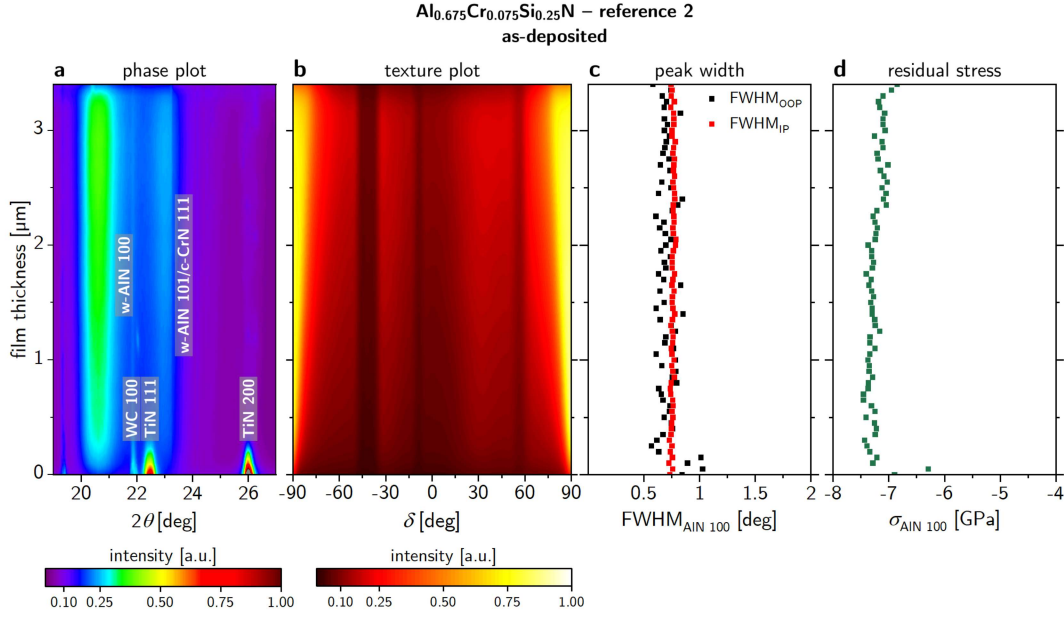


Figure 3.10: CSnanoXRD data retrieved from the as-deposited Al_{0.675}Cr_{0.075}Si_{0.25}N film. In (a) the phase plot obtained by an azimuthal integration of the corresponding Debye-Scherrer rings is shown, while in (b) the azimuthal distribution of the diffracted intensities indicates $\langle 110 \rangle$ fibre texture. The cross-sectional FWHM of the AlN 100 peak reveals equiaxial nanocrystallites with a size of ~ 7 nm (c). The residual stress evaluated from the AlN 100 Debye-Scherrer ring shows an oscillatory variation around a mean value of ~ -7.5 GPa (d).

In order to analyse the texture, again the azimuthal intensity distribution of the AlN 100 Debye-Scherrer ring was evaluated. A $\langle 110 \rangle$ fibre texture was revealed in the as-deposited thin film, *cf.* texture plot in Fig. 3.10b where an increased intensity is observed for an azimuthal angle δ of ~ 30 deg. After the heat-treatment the azimuthal intensity distributions did not change, indicating a stable $\langle 110 \rangle$ fibre texture in the thin film. It has to be noted that the vertically oriented lines with a low intensity in the depth-resolved texture plots in Figs. 3.10b and 3.11b are due to the segmented detector design, *cf.* Fig. 2.4.

Constant and uniform FWHM results for both out-of-plane and in-plane orientation were measured in the as-deposited sample Fig. 3.10c. They reveal equiaxial nanocrystallites with a size of ~ 7 nm. FWHM was increased for both orientations as a result of the applied heat-treatment, *cf.* Fig. 3.11c. In the as-deposited Al_{0.675}Cr_{0.075}Si_{0.25}N thin film residual stress analysis revealed compressive residual stresses that amount to ~ -7.5 GPa. Depth-resolved residual stress in the heat-treated thin film confirms stress relaxation induced by the annealing and leads to a decrease of the compressive residual stresses to a level of about -4 to -3.5 GPa.

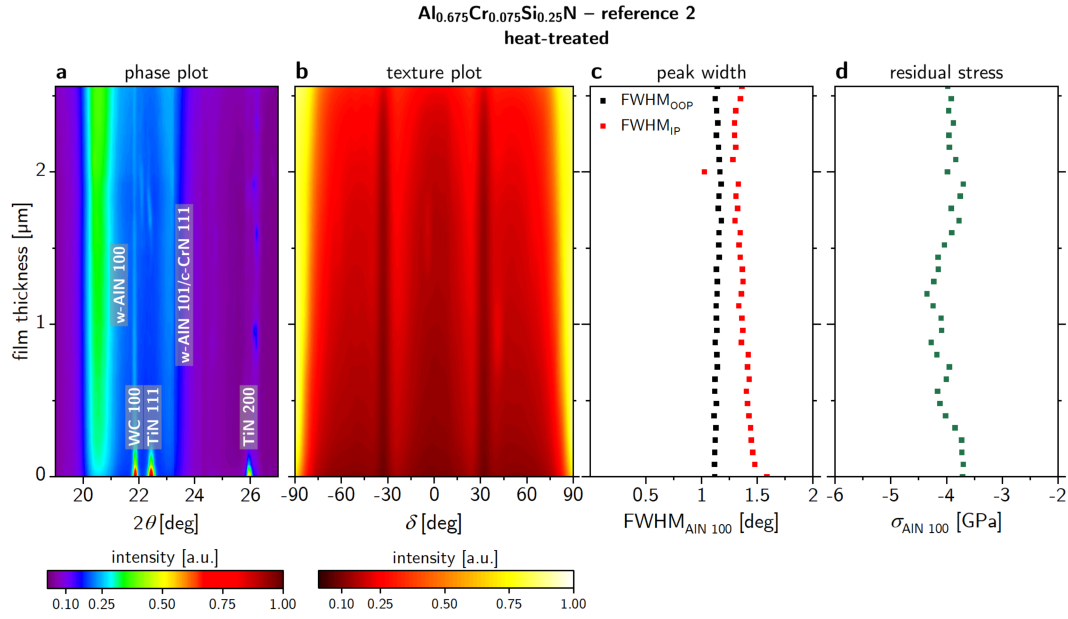


Figure 3.11: CSnanoXRD data retrieved from the heat-treated Al_{0.675}Cr_{0.075}Si_{0.25}N film. In (a) the phase plot obtained by an azimuthal integration of the corresponding Debye-Scherrer rings is shown, while in (b) the azimuthal distribution of the diffracted intensities indicates $\langle 110 \rangle$ fibre texture. The cross-sectional FWHM of the AlN 100 peak is increased with respect to the as-deposited condition (c). The residual stress evaluated from the AlN 100 Debye-Scherrer ring shows an oscillatory variation in a range of ~ -4 to -3.5 GPa (d).

3.3.3 AlCrSiN multilayer thin film

Cross-sectional X-ray nanodiffraction applied to the as-deposited sample shows w-AlN 100, 002 and 101 peaks, the latter supposedly overlaps with the c-CrN 111 reflection, *cf.* Fig. 3.12a. Therein, the fluctuating intensities of the overlapping w-AlN 101 and c-CrN 111 peaks can nicely be correlated to the intermittent multilayer structure. The reflections are more pronounced for the thicker intermediate layers (Al_{0.63}Cr_{0.27}Si_{0.1}N) in comparison with the thinner layers (Al_{0.675}Cr_{0.075}Si_{0.25}N) as the latter contain more Si and thus the content of a-Si_xN_y matrix is higher. The obtained phase plot from the as-deposited AlCrSiN multilayer thin film in Fig. 3.12a is in agreement with the monolithic counterparts presented in Figs. 3.8a and 3.10a. The bonding layer is represented by the TiN 111 and 200 peaks in Fig. 3.12a. After the heat-treatment the sequential intensity distribution along the cross-section diminishes, *cf.* Fig. 3.13a. Please note that the heat-treated sample was measured with a higher photon energy than the as-deposited sample. Thus, the wurtzite AlN 100, 002 and 101 peaks can be observed at $2\theta = 17.4$, 18.9 and 19.8 deg, respectively. The c-CrN 111 peak overlaps with the w-AlN 101 peak

and the c-CrN 200 peak is found at $2\theta = 22.7$ deg. As in the as-deposited condition the TiN 111 and 100 peaks directly between substrate and thin film indicate the bonding layer in the heat-treated sample. WC 001 and 100 reflections were measured across the whole thin film which may be the consequence of substrate material being redeposited on the cross-section of the thin film during the sample preparation by femto-second laser ablation [74, 75].

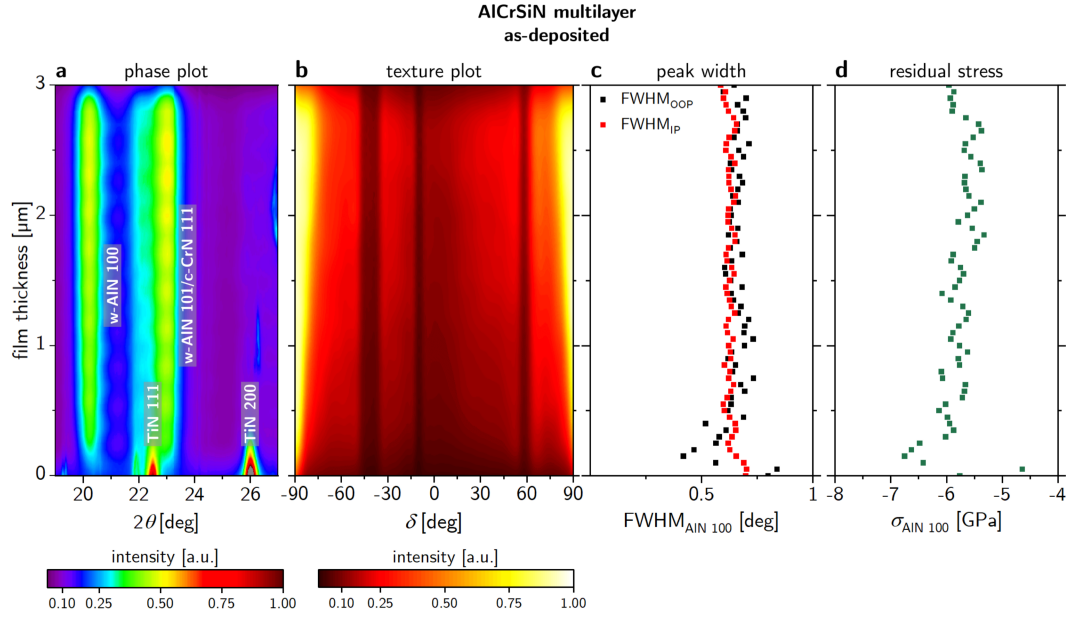


Figure 3.12: CSnanoXRD data retrieved from the as-deposited AlCrSiN multilayer thin film. In (a) the phase plot obtained by an azimuthal integration of the corresponding Debye-Scherrer rings is shown, while in (b) the azimuthal distribution of the diffracted intensities indicates no preferred orientation in the multilayer. The cross-sectional FWHM of the AlN 100 peak indicates uniform domain sizes in both sublayers (c). The residual stress evaluated from the AlN 100 Debye-Scherrer ring periodically varies between ~ 6 and ~ 5.5 GPa in the thicker and thinner sub-layer, respectively (d).

Neither the as-deposited (Fig. 3.12b) nor the heat-treated (Fig. 3.13b) sample indicated a clear intensity enhancement at a certain angle in the texture plot. Consequently, in contrast to the monolithic thin films, texture in the multilayer thin film remains inconclusive.

Analysis of the peak broadening in as-deposited state revealed an oscillating FWHM with a mean value of ~ 0.6 deg representing the multilayer periodicity of the investigated thin film, *cf.* Fig. 3.12c. After the heat treatment, a decrease in the FWHM was observed for both out-of-plane and in-plane orientations, averaging approximately 0.4 deg, *cf.* Fig. 3.13c. In the in-plane orientation the oscillatory nature of the FWHM remained

intact. The decrease of the average FWHM can be attributed to the annihilation of dislocations as well as a relaxation of lattice distortions [13, 57].

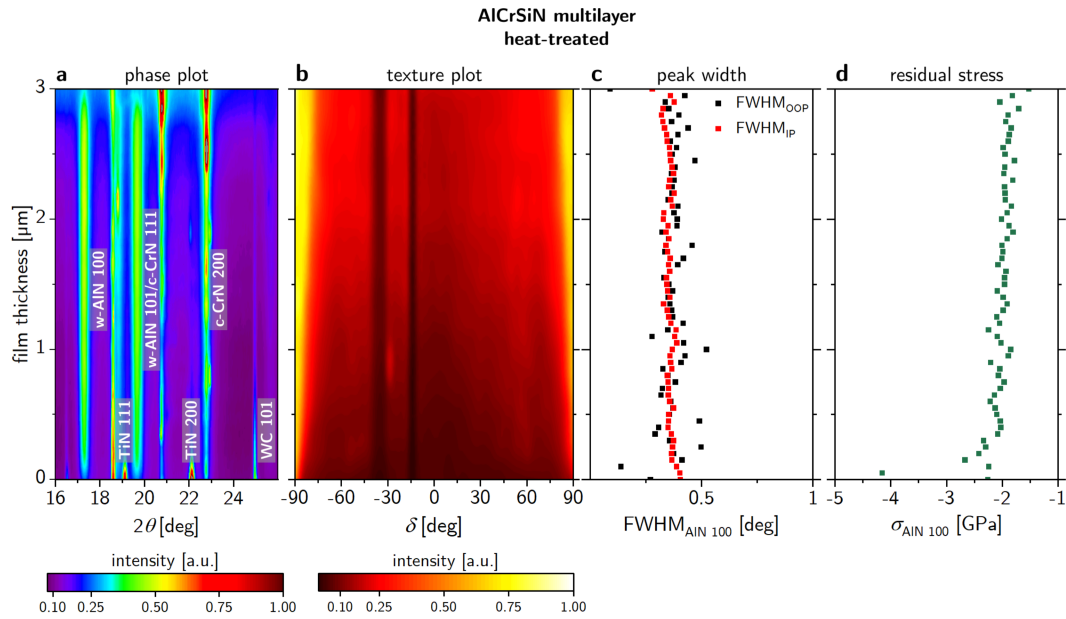


Figure 3.13: CSnanoXRD data retrieved from the heat-treated AlCrSiN multilayer thin film. In (a) the phase plot obtained by an azimuthal integration of the corresponding Debye-Scherrer rings is shown, while in (b) the azimuthal distribution of the diffracted intensities texture remained inconclusive. The cross-sectional FWHM of the AlN 100 peak indicates uniform domain sizes in both sublayers (c). The residual stress evaluated from the AlN 100 Debye-Scherrer ring shows an oscillatory variation around a mean value of ~ -2 GPa (d).

As shown in Fig. 3.12d the cross-sectional stress distribution correlates with the intermittent multilayer structure. Compressive residual stresses of about -6 GPa and -5.5 GPa were evaluated in the thicker and thinner sublayers of the multilayer, respectively. In both layers the residual stresses slightly decrease in growth direction, a trend that is even more pronounced after the heat-treatment, *cf.* Fig. 3.13d. Moreover, the variation of stresses between the two intermittent layers is reduced in the annealed sample. At elevated temperatures defect annihilation leads to stress relaxation [73], clearly shown here with the residual stresses being reduced down to about -2 GPa.

3.4 Mechanical properties obtained by *in situ* microcantilever bending

3.4.1 Characterization of Young's modulus, fracture stress and fracture toughness

Using the relationships derived in sections 2.6.2 to 2.6.4, the recorded load-displacement data were transformed into stress-displacement and K_I -displacement data, respectively.

For the $\text{Al}_{0.63}\text{Cr}_{0.27}\text{Si}_{0.1}\text{N}$ thin film, a total of 14 cantilevers were evaluated in the as-deposited condition, half of which were notched. Ten cantilevers were tested in the heat-treated condition, three of which were notched. Only representative curves are shown in Fig. 3.14 for ease of viewing.

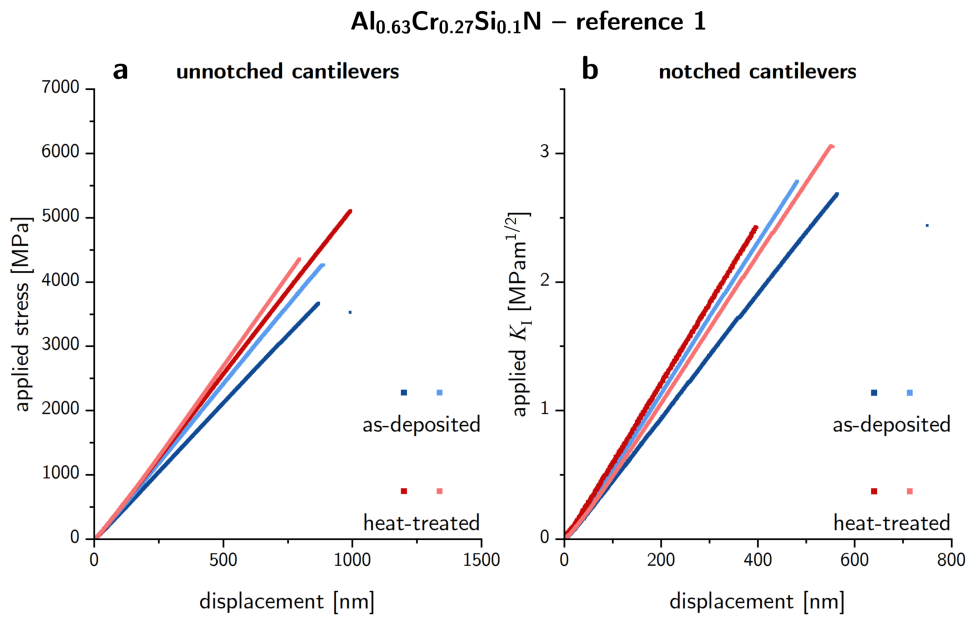


Figure 3.14: Results from microcantilever bending tests for the $\text{Al}_{0.63}\text{Cr}_{0.27}\text{Si}_{0.1}\text{N}$ monolithic thin film calculated from the load-displacement data. In (a), the applied stress-displacement curves obtained from two representative unnotched cantilevers both for as-deposited and heat-treated conditions are shown, while in (b) the applied K_I -displacement for representative notched cantilevers in both sample conditions is displayed.

As listed in Table 3.1, heat-treatment results in an increase in Young's modulus and fracture stress compared to the as-deposited condition. However, as a consequence of the high intrinsic scattering due to the defects in the thin film, *cf.* Figs. 3.1 and 3.2, the increase of Young's modulus and fracture stress are not significant. Additionally,

fracture toughness was also slightly increased by the annealing treatment, consistent with the findings by Ziegelwanger [46].

Table 3.1: Mechanical properties of the $\text{Al}_{0.63}\text{Cr}_{0.27}\text{Si}_{0.1}\text{N}$ thin film evaluated from bending tests on unnotched and notched cantilevers.

$\text{Al}_{0.63}\text{Cr}_{0.27}\text{Si}_{0.1}\text{N}$ reference 1	Young's modulus [GPa]	fracture stress [GPa]	fracture toughness [MPa·m ^{1/2}]
as-deposited	230 ± 32	4.0 ± 0.6	2.5 ± 0.3
heat-treated	246 ± 45	4.4 ± 0.9	2.7 ± 0.4

For the second reference thin film, cantilevers were prepared from $\text{Al}_{0.675}\text{Cr}_{0.075}\text{Si}_{0.25}\text{N}$ as-deposited and heat-treated thin films. Eight cantilevers were measured for each condition, with half of them featuring notches. The evaluated curves are shown in Fig. 3.15, two cantilevers failed prior to testing.

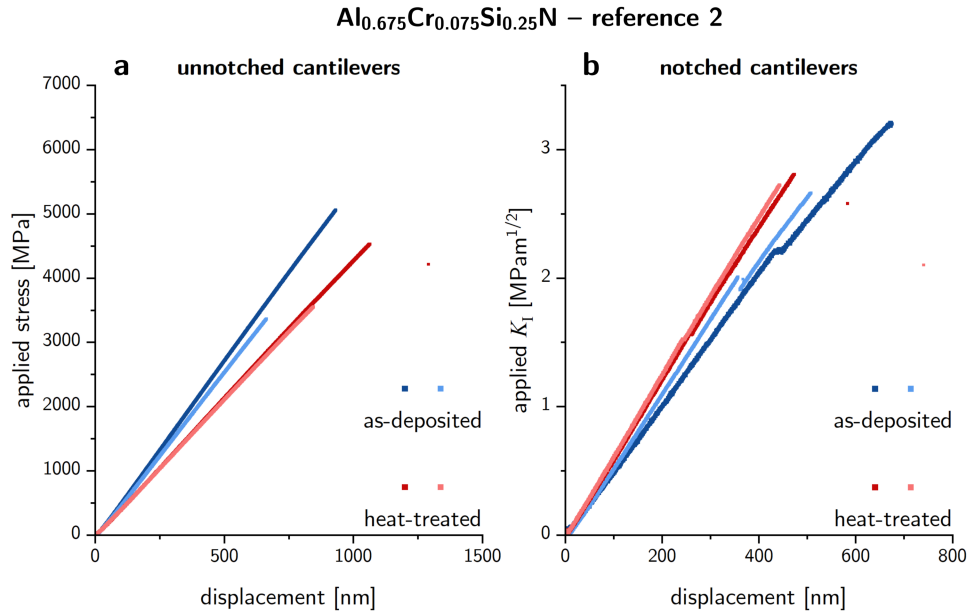


Figure 3.15: Results from microcantilever bending tests for the $\text{Al}_{0.675}\text{Cr}_{0.075}\text{Si}_{0.25}\text{N}$ monolithic thin film calculated from the load-displacement data. In (a), the applied stress-displacement curves from two representative unnotched cantilevers are presented for both as-deposited and heat-treated conditions, while in (b) the applied K_I -displacement for representative notched cantilevers in both sample conditions is displayed.

Contrary to $\text{Al}_{0.63}\text{Cr}_{0.27}\text{Si}_{0.1}\text{N}$, heat-treatment resulted in a decrease in both the Young's modulus and fracture stress in the $\text{Al}_{0.675}\text{Cr}_{0.075}\text{Si}_{0.25}\text{N}$ thin film. In detail,

Young's modulus was significantly reduced by $31 \pm 20\%$, while the fracture stress decrease was insignificant due to the high intrinsic errors that were observed especially for the as-deposited cantilevers. On the contrary, the fracture toughness remained constant after annealing, *cf.* Table 3.2.

Table 3.2: Mechanical properties of the $\text{Al}_{0.675}\text{Cr}_{0.075}\text{Si}_{0.25}\text{N}$ thin film evaluated from bending tests on unnotched and notched cantilevers.

$\text{Al}_{0.675}\text{Cr}_{0.075}\text{Si}_{0.25}\text{N}$ reference 2	Young's modulus [GPa]	fracture stress [GPa]	fracture toughness [MPa·m ^{1/2}]
as-deposited	310 ± 30	4.9 ± 1.4	2.8 ± 0.4
heat-treated	215 ± 60	4.0 ± 0.5	2.8 ± 0.2

Finally, the results for the AlCrSiN multilayer thin film are presented. Again, eight cantilevers, four notched and four unnotched, were tested for both the as-deposited and heat-treated condition. The corresponding stress-displacement and stress intensity-displacement curves are presented in Fig. 3.16. One unnotched cantilever failed during the preparation of the bending test.

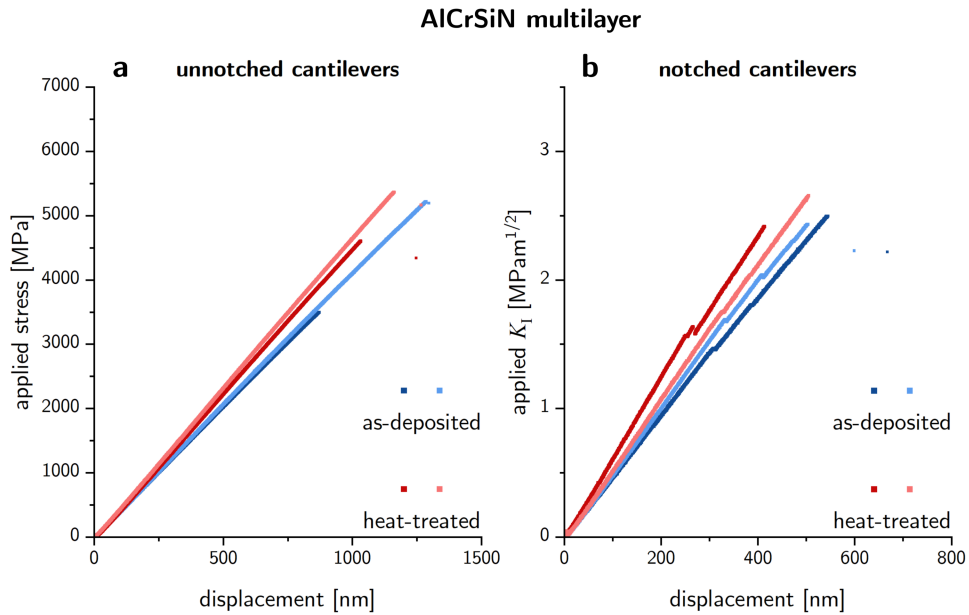


Figure 3.16: Results from microcantilever bending tests for the multilayer. In (a) the maximum applied tensile stress-displacement curves, which were obtained from unnotched cantilevers, are shown. Stress intensity-displacement curves, that were retrieved from notched cantilevers, are plotted in (b). In both graphs, representative curves are shown for both the as-deposited and heat-treated conditions.

As evident from the data presented in Table 3.3, heat-treatment resulted in an increase of Young's modulus and fracture stress. However, it is noteworthy that the heat-treatment seemingly led to a slight reduction in the fracture toughness of the multilayered thin film.

Table 3.3: Mechanical properties of the multilayer thin film evaluated from microcantilever bending tests on unnotched and notched cantilevers.

AlCrSiN multilayer	Young's modulus [GPa]	fracture stress [GPa]	fracture toughness [MPa·m ^{1/2}]
as-deposited	216 ± 50	4.1 ± 0.9	2.7 ± 0.2
heat-treated	277 ± 82	4.9 ± 0.5	2.5 ± 0.2

3.4.2 Qualitative analysis of the fracture surfaces after microcantilever bending

In this section the *ex situ* SEM analysis of the fracture surfaces after the microcantilever bending tests is presented and shortly discussed.

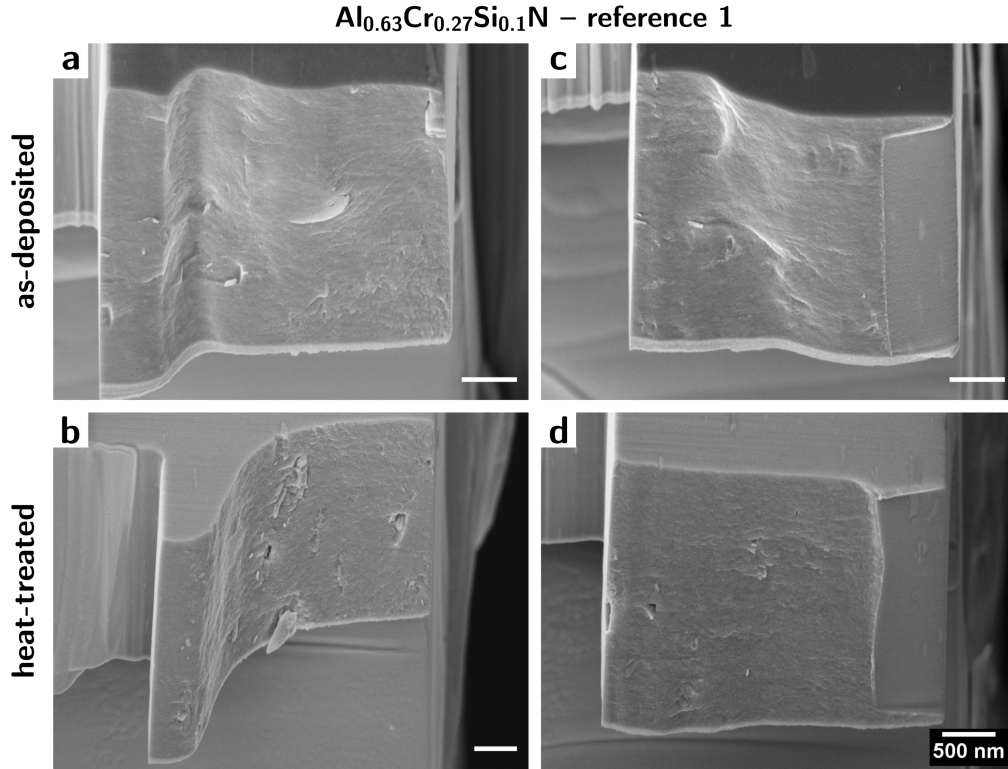


Figure 3.17: Fracture surfaces of unnotched (a, b) and notched (c, d) $\text{Al}_{0.63}\text{Cr}_{0.27}\text{Si}_{0.1}\text{N}$ cantilevers imaged *ex situ* in the SEM after the bending tests. The length of the scale bars in (a-c) corresponds to 500 nm.

The micrographs of the $\text{Al}_{0.63}\text{Cr}_{0.27}\text{Si}_{0.1}\text{N}$ cantilevers fracture surfaces are presented in Fig. 3.17. A clear difference can be drawn from the observed fracture behaviour, since the fracture path across the unnotched cantilever in as-deposited state (Fig. 3.17a) is rather straight, compared to the curved appearance of the fracture surface in the heat-treated state (Fig. 3.17b). Contrary, in the notched cantilevers, there is no clear evidence of a change in fracture morphology (*cf.* Figs. 3.17c and d). In agreement with findings from literature [13] and together with the precipitates observed in SEM (Fig. 3.2d) and TEM (Fig. 3.3) it can be deduced that the precipitates formed during heat-treatment change the fracture morphology of the $\text{Al}_{0.63}\text{Cr}_{0.27}\text{Si}_{0.1}\text{N}$ thin film. This is also corroborated by the slight increase in Young's modulus and fracture stress upon heat-treatment, *cf.* Table 3.1.

$\text{Al}_{0.675}\text{Cr}_{0.075}\text{Si}_{0.25}\text{N}$ – reference 2

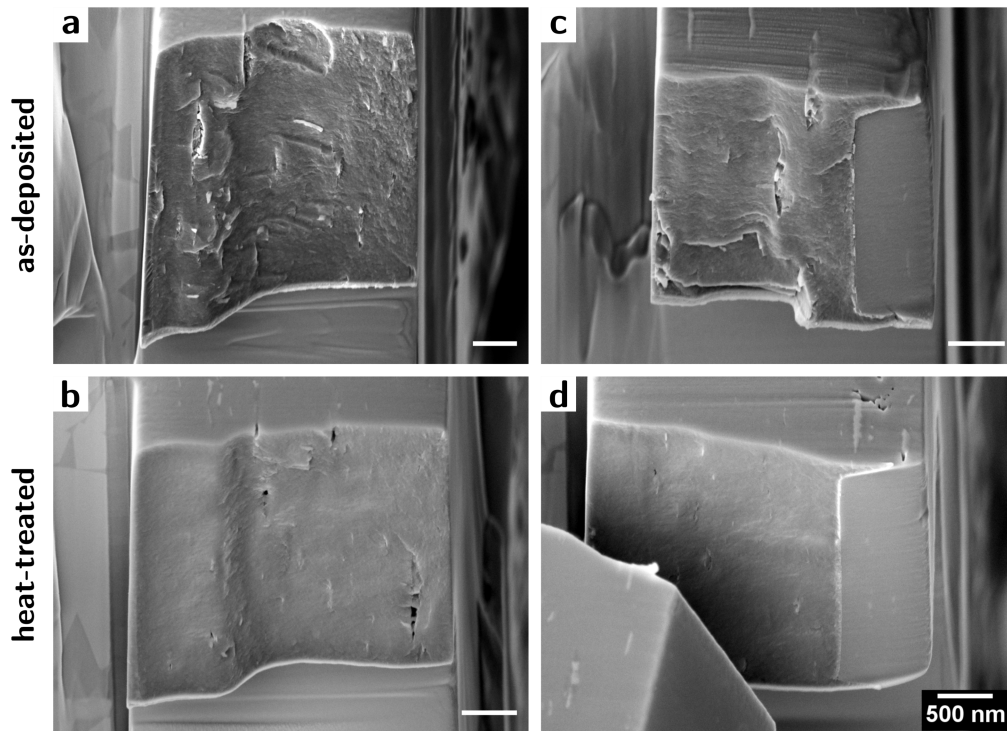


Figure 3.18: Fracture surfaces of unnotched (a, b) and notched (c, d) $\text{Al}_{0.675}\text{Cr}_{0.075}\text{Si}_{0.25}\text{N}$ cantilevers imaged *ex situ* in the SEM after the bending tests. The length of the scale bars in (a-c) corresponds to 500 nm

Contrary, no deviation from a relatively linear fracture path, typically associated with intercolumnar or intercrystalline fracture, was observed for the cantilevers milled from the $\text{Al}_{0.675}\text{Cr}_{0.075}\text{Si}_{0.25}\text{N}$ film as shown in Fig. 3.18. In contrast to the $\text{Al}_{0.63}\text{Cr}_{0.27}\text{Si}_{0.1}\text{N}$ film, the $\text{Al}_{0.675}\text{Cr}_{0.075}\text{Si}_{0.25}\text{N}$ thin film was proven to be devoid of any precipitate formation and structural changes, as shown by SEM (Figs. 3.1c and f, Figs. 3.2c and f), TEM (Fig. 3.4) and CSnanoXRD (Figs. 3.10 and 3.11). The concomitant deficiency in grain boundary cohesion could be a reason that the crack is not deflected during the fracture event and straight fracture surfaces are observed in Fig. 3.18.

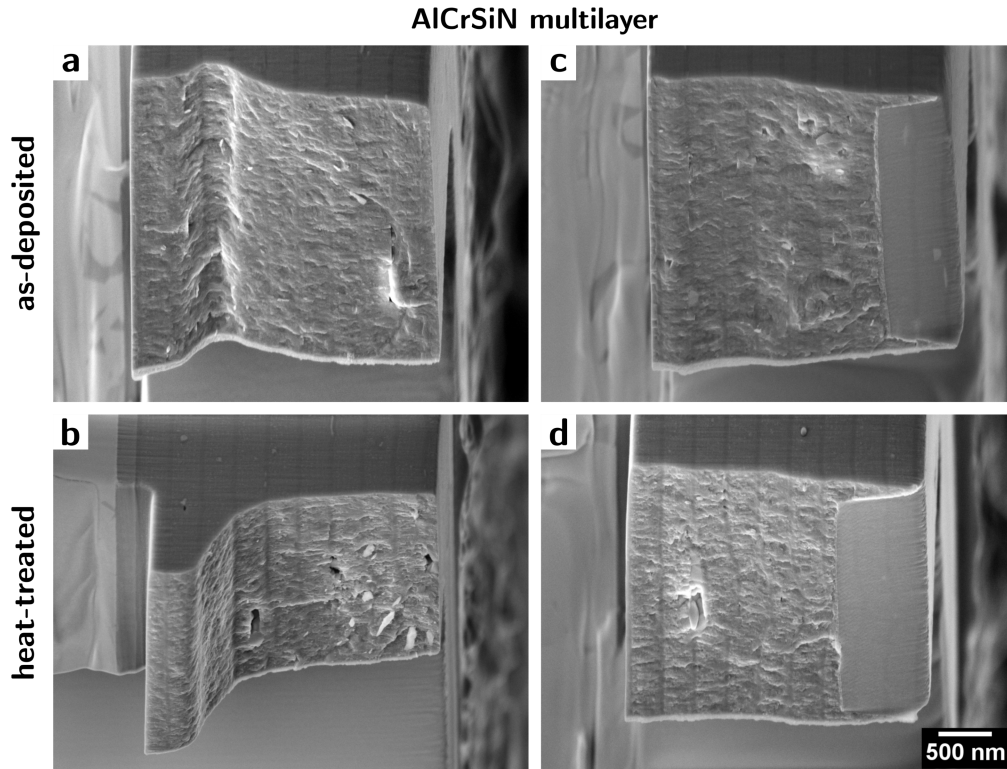


Figure 3.19: Fracture surfaces of unnotched (a, b) and notched (c, d) AlCrSiN multilayer cantilevers imaged *ex situ* in the SEM after the bending tests. The scale bar applies to all micrographs.

The micrographs of the fracture surfaces from unnotched cantilevers, that were fabricated from the AlCrSiN multilayer thin film, indicate the transition from a straight (Fig. 3.19a) to a curved appearance of the fracture surface (Fig. 3.19b). This change in fracture behaviour is attributed to the increasing cohesive energy of the grain boundaries due to precipitation of c-Cr(Al)N upon heat-treatment in the ~250 nm thick $\text{Al}_{0.63}\text{Cr}_{0.27}\text{Si}_{0.1}\text{N}$ sublayers. The c-Cr(Al)N precipitates were also confirmed by SEM (Figs. 3.2a and d), TEM (Figs. 3.6 and 3.7) as well as CSnanoXRD (Figs. 3.12 and 3.13) and effectively alter the fracture morphology as already discussed for Figs. 3.17a and b.

3.4.3 Evaluation of stepwise crack propagation in the heat-treated AlCrSiN multilayer

Closer examination of the load-displacement curves of the heat-treated AlCrSiN multilayer reveals a load drop and a concomitant reduced slope in the load-displacement curve, *cf.* Fig. 3.20.

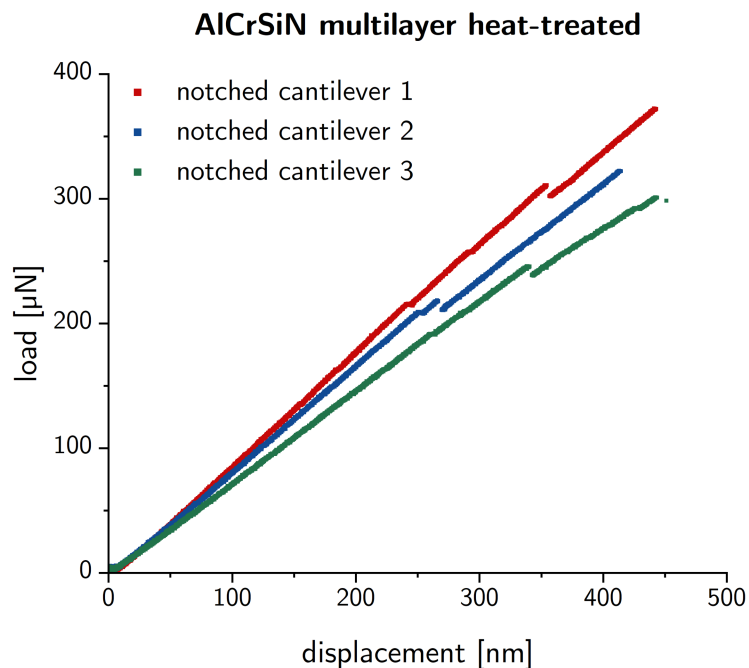


Figure 3.20: Load-displacement curves recorded during the *in situ* bending tests on notched microcantilevers of the heat-treated AlCrSiN multilayer thin film. Clearly visible in all three depicted curves are discontinuities where the linearly progressing curve exhibits a drop in load. After the load drop, the slope is also decreased for all three load-displacement curves.

This decreasing slope is indicative of a reduction in cantilever stiffness, while the decrease in load can be interpreted as a crack propagation event [67]. The regions of interest from all three curves in Fig. 3.20 are depicted in Fig. 3.21 in order to emphasise on the assumed crack propagation event. Comparison of the microcantilever stiffnesses before and after the load drop, k_1 and k_2 , respectively, revealed a decrease of about 10%.

As described in Sec. 2.6.5, a change in stiffness from k_1 to k_2 allows for an analytical evaluation of the correlating crack length a before and after the crack propagation event, respectively. Consequently, by evaluating Eq. 2.31 for all three notched cantilevers the respective crack lengths were calculated and subtracted from each other to yield the analytically evaluated crack propagation $\Delta a_{analytical}$. In Fig. 3.22 the correlation between

the crack length a and the cantilever stiffness k resulting from Eq. 2.31 is plotted exemplary for the notched cantilever 3. The analytical evaluation procedure required the stiffness of an unnotched cantilever k_0 . Bending tests on unnotched microcantilevers of the heat-treated multilayer revealed a Young's modulus E of ~ 280 GPa, k_0 was then calculated from E and each of the cantilevers geometries.

In order to verify the analytical solution the fracture surfaces of the microcantilevers were imaged *ex situ* in the SEM. In the micrographs the notch depth was measured at several positions to get a mean initial crack length. At the same positions the distance from the notch tip to the next interface of a high Si-containing was measured, the mean value is interpreted as Δa_{image} , cf. Fig. 3.22a.

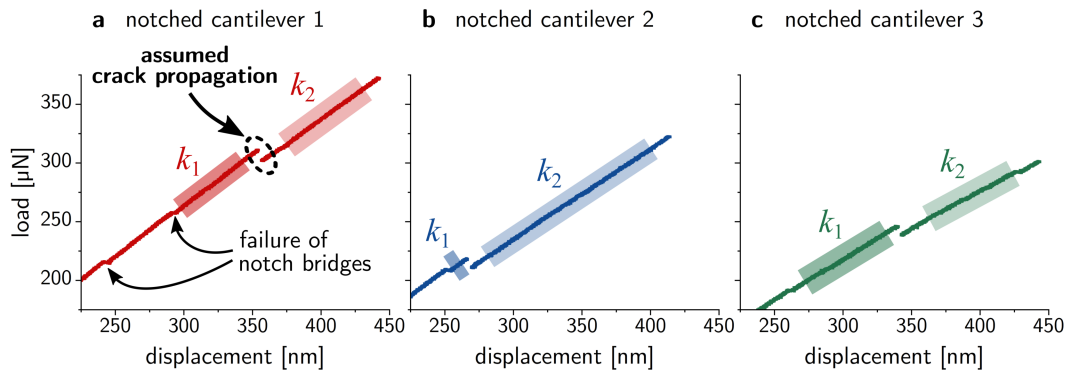


Figure 3.21: Load-displacement curves recorded during microcantilever bending tests of the heat-treated AlCrSiN multilayer thin film are depicted with a focus on the region where the load drop is observed. Prior to the significant load drop that leads to an intermittence in the load-displacement curve (encircled for notched cantilever 1), minor load drops are observed in (a) which are attributed to the failure of notch bridges. Due to a non-perfect sample fabrication and cantilever loading, the two bridges do not break at the exact same load. The shaded area marks the region where a linear fit of the curve was carried out in order to determine k_1 and k_2 , the stiffness of the notched microcantilever before and after the load drop, respectively.

The results for $\Delta a_{analytical}$ and Δa_{image} are given in Table 3.4. For cantilever 1 a larger deviation between $\Delta a_{analytical}$ and Δa_{image} is observed. Here it has to be noted that the fracture surface was only partly visible as it was covered by the fractured cantilever. Possible deviations in the distance between notch tip and next interface could therefore not be assessed. Following the results from cantilevers 2 and 3 the assumed stepwise crack propagation could indeed be confirmed by matching results from both the analytical evaluation and SEM imaging of the fracture surface.

evaluation of crack propagation
notched cantilever 3

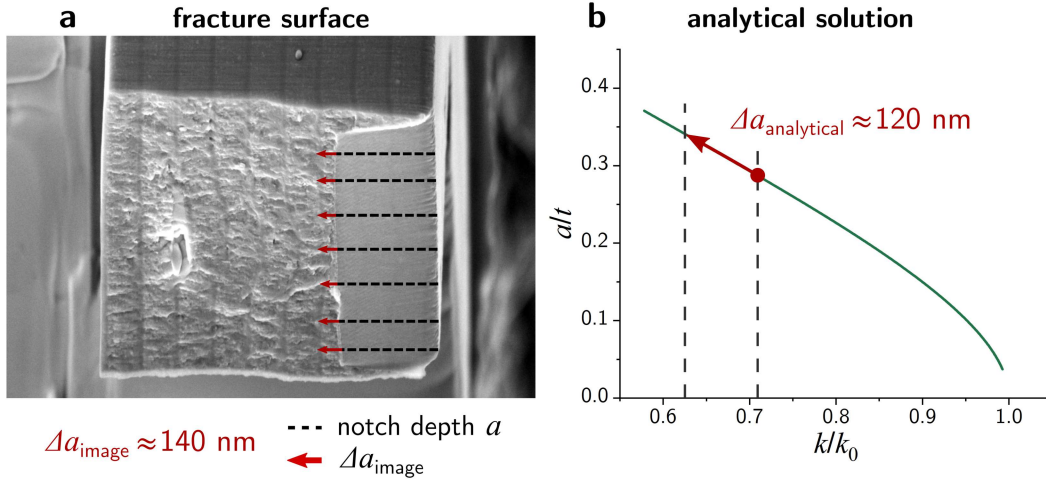


Figure 3.22: The fracture surface of the microcantilever was imaged ex situ in the SEM. At several positions the notch depth and the distance from the notch tip to the interface of the low Si-containing interface was measured (a). The mean value is interpreted as Δa_{image} . The analytical solution as described in Sec. 2.6.5 correlates the crack length a to the stiffness k and allows for an evaluation of $\Delta a_{analytical}$ (b). In this case the cantilever thickness t was $2.69 \mu\text{m}$, k_0 was calculated from a Young's modulus of $\sim 280 \text{ GPa}$ that was determined in bending tests on unnotched cantilevers.

Table 3.4: Evaluated crack propagation for the three notched cantilevers of the heat-treated AlCrSiN multilayer.

cantilever	$\Delta a_{analytical}$ [nm]	Δa_{image} [nm]
1	91	200
2	54	50
3	140	120

As the fracture toughness depends on the crack length a , *cf.* Eq. 2.25, the fracture toughness had to be reevaluated after the confirmation of a propagating crack in the heat-treated AlCrSiN multilayer. The resulting fracture toughness values are displayed in Fig. 3.23. Therein the characteristic behaviour of a resistance-curve that is also referred to as *R-curve* and typically encountered in tough ceramics can be observed [7]. The confirmed stepwise crack propagation and concomitant increase in fracture toughness revealed the extrinsic toughening in the multilayer thin film that was induced by a cross-sectional variation of layers with and without precipitates.

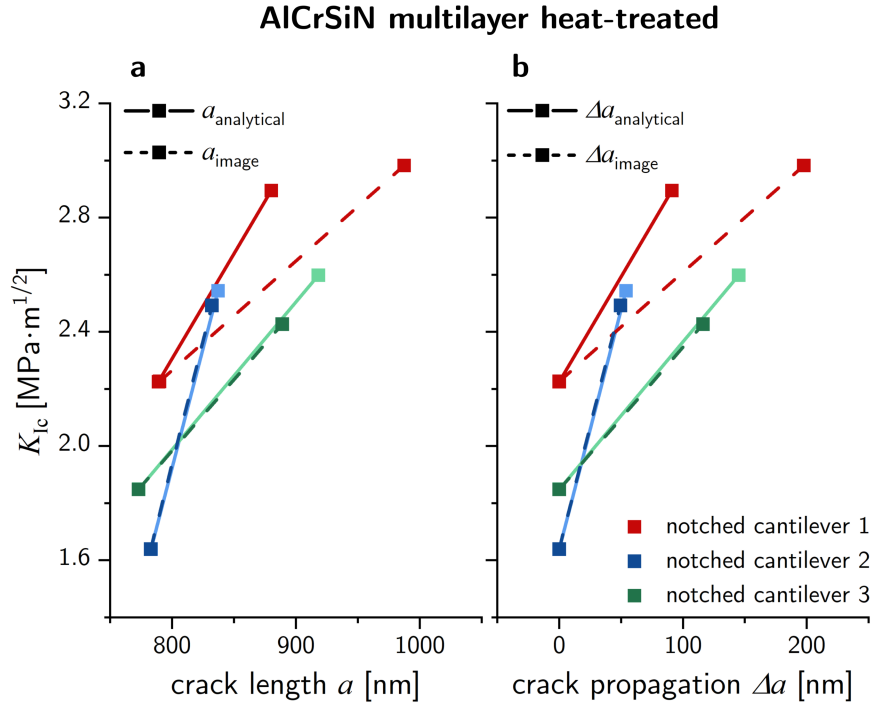


Figure 3.23: Following the bending tests, the crack lengths of three notched cantilevers for the heat-treated multilayer were evaluated both analytically and from fracture surfaces. The results from both approaches are in good agreement and indicate stepwise crack propagation and a concomitant increase in fracture toughness. The graph in (b) shows a crack propagation resistance curve, also known as *R-curve*, with a rising K - Δa behaviour.

As shown in Fig. 3.23 the crack propagation in cantilevers 2 and 3 led to a concomitant increase in fracture toughness from ~ 1.6 to ~ 2.5 MPa·m^{1/2} and from ~ 1.8 to ~ 2.5 MPa·m^{1/2}, respectively. For cantilever 1 the analytical evaluation of the crack length and the crack length from SEM analysis at the fracture surface show a discrepancy, the reason for that was discussed above. Consequently, also the fracture toughness values of cantilever 1 show a mismatch, *cf.* Fig. 3.23. Nevertheless, a stepwise crack propagation and significant increase in fracture toughness was also observed for this cantilever.

4

Discussion

4.1 Microstructural evolution of the thin films upon heat-treatment

As shown in this study, the interplay between the thin film composition and the applied heat-treatment was carefully adjusted in order to obtain a multilayered AlCrSiN thin film with a cross-sectional variation of the microstructure. The characterization by SEM, TEM and CSnanoXRD elucidated the correlation between the microstructure of the AlCrSiN multilayer thin film and the microstructural evolution of the reference monolithic thin films before and after the heat-treatment.

SEM analysis conducted on FIB-polished cross-sections of the monolithic reference $\text{Al}_{0.63}\text{Cr}_{0.27}\text{Si}_{0.1}\text{N}$ thin film revealed a layered microstructure with interfaces aligned parallel to the substrate surfaces, *cf.* Figs. 3.2a and d. As confirmed by TEM analysis (Fig. 3.3), the periodicity of these sublayers is about ~ 30 nm and they are enriched with Cr in the as-deposited state. Remarkably, the same substructure was observed within the sublayers of the multilayered film with similar composition (Figs. 3.2b and e). The appearance of such a periodic substructure is commonly associated with thin films deposited by cathodic arc evaporation [72, 76, 77].

As illustrated by SEM (Fig. 3.2d) and TEM (Fig. 3.3), subjecting the $\text{Al}_{0.63}\text{Cr}_{0.27}\text{Si}_{0.1}\text{N}$ to the heat-treatment resulted in the formation of precipitates primarily located at the interfaces between the sublayers. Through the EDS analysis in the TEM, these precipitates were identified as globular $\text{Cr}_x\text{Al}_y\text{N}$ precipitates with $x \sim 0.5$ (Fig. 3.7), indicating the formation of the cubic Cr(Al)N phase. Further evidence for the presence of the c-Cr(Al)N phase is given by CSnanoXRD analysis, where the intensity of the CrN 200 peak significantly increased after the heat-treatment, *cf.* Figs. 3.8a and 3.9a. As demonstrated in Ref. [46], a low Si content does not impede precipitation from the w-Al(Cr)N phase during annealing at 1050°C. Similar processes were observed in the multilayered thin films, where precipitates formed within the Cr-enriched sublayers, that, in turn, originated from the cathodic arc evaporation process [72, 76, 77]. The

observed formation of cubic precipitates upon heat-treatment aligns with experimental data found in literature for TMN thin films possessing a wurtzite crystal structure [13, 28, 46]. As reported there, precipitation was evidenced for $\text{Al}_{0.9}\text{Cr}_{0.1}\text{N}$, $\text{Al}_{0.8}\text{Cr}_{0.2}\text{N}$ as well as $\text{Al}_{0.63}\text{Cr}_{0.27}\text{Si}_{0.1}\text{N}$ after annealing up to 1100°C .

Quite contrary to the $\text{Al}_{0.63}\text{Cr}_{0.27}\text{Si}_{0.1}\text{N}$ monolithic thin film, the formation of a Cr-enriched substructure was not observed in the case of $\text{Al}_{0.675}\text{Cr}_{0.075}\text{Si}_{0.25}\text{N}$ reference film, *cf.* Figs. 3.2c and f. TEM analysis revealed no evidence of precipitation formation and TEM-EDS analysis indicated a uniform distribution of chemical elements within the thin film (Fig. 3.4). In analogy to ZrAlN thin films [78], where the onset of precipitation was shifted to higher temperatures with increasing Al content, it can be concluded that the higher Al/Cr ratio of the $\text{Al}_{0.675}\text{Cr}_{0.075}\text{Si}_{0.25}\text{N}$ thin film delays the precipitation. Similarly, the decomposition of AlCrN thin films is delayed by addition of Si, as shown by Jäger *et al.* [34], thus strengthening the thermal stability of the $\text{Al}_{0.675}\text{Cr}_{0.075}\text{Si}_{0.25}\text{N}$ thin film. Furthermore, CSnanoXRD analysis of the $\text{Al}_{0.675}\text{Cr}_{0.075}\text{Si}_{0.25}\text{N}$ thin film revealed the exclusive presence of the w-Al(Cr)N crystalline phase in both the as-deposited state (Fig. 3.10a) and after the heat-treatment (Fig. 3.11a).

Considering the monolithic counterparts of the multilayered AlCrSiN thin films, the conditions necessary for the cross-sectional alternation of precipitation-enhanced and precipitation-free sublayers are given. Indeed, upon subjecting the multilayered AlCrSiN thin film to the heat-treatment, alternating sublayers with and without precipitates were found by TEM analysis (Figs. 3.5 and 3.7). According to the available literature [13, 46], precipitates allow for a transition in fracture morphology from inter- to transcrystalline. Consequently, a multilayer microstructure with a cross-sectional variation in fracture morphology has been successfully assembled. In the following section, the implications of this microstructure on the fracture properties will be discussed.

4.2 Extrinsic toughening by sequential application of precipitation-based grain boundary design

The correlative nanoscale characterization has revealed that the heat-treatment at 1050°C for 5 min resulted in the formation of alternating sublayers with and without c-Cr(Al)N precipitates within the AlCrSiN multilayer thin film (Figs. 3.2b and e, Fig. 3.5). In agreement with experimental data from Refs. [25, 33] that the c-Cr(Al)N phase is considerably harder and stiffer compared to the w-Al(Cr)N phase, a cross-sectional variation in hardness and stiffness was therefore anticipated for the heat-treated AlCrSiN multilayer investigated in this thesis.

The evaluation of the microcantilever bending tests in Sec. 3.4.3 revealed that the sequentially varying mechanical properties effectively influenced the crack propagation behaviour, thereby providing extrinsic toughening to the multilayered AlCrSiN thin film. Both an analytical solution based on the changing stiffness of a notched cantilever and SEM analysis of the fracture surfaces yielded consistent results, confirming a singular stepwise crack propagation in the range of ~50-150 nm, as presented in Table 3.4. This observation confirms that prior to the final fracture event of the cantilever the crack is arrested at the adjacent interface devoid of c-Cr(Al)N precipitates.

The crack propagation concurrently led to a significant increase in the evaluated fracture toughness, with values increasing by 40-50%, reaching values of ~2.5 and even ~3.0 MPa·m^{1/2}, as shown in Fig. 3.23. The fracture toughness of the heat-treated reference thin films measured to 2.7 ± 0.4 and 2.8 ± 0.2 MPa·m^{1/2} for Al_{0.63}Cr_{0.27}Si_{0.1}N and Al_{0.675}Cr_{0.075}Si_{0.25}N, respectively, *cf.* Tables 3.1 and 3.2. However, it is crucial to emphasize that only the heat-treated multilayer thin film exhibited an unprecedented stepwise crack propagation and a concomitant *R-curve* behaviour, observed in Fig. 3.23, as a result of extrinsic toughening.

Experimental data from microcantilever bending tests, as reported by Meindlhumer *et al.*, document a fracture toughness of 3.0 ± 0.2 MPa·m^{1/2} for a heat-treated monolithic w-Al_{0.9}Cr_{0.1}N thin film [13]. In their study, the beneficial enhancement of fracture toughness by heat-treatment is attributed to the formation globular c-Cr(Al)N precipitates at grain boundaries altering the fracture mechanism from inter- to trans-granular. A similar concept can be considered for interpreting the extrinsic toughening observed in the AlCrSiN multilayer investigated in this thesis. It is important to note, however, that the thin film microstructure examined in Ref. [13] consisted of coarse columnar grains, in contrast to the nanocomposite microstructure analysed in this thesis.

Similar micromechanical bending tests were conducted on a comparable nanocomposite AlCrSiN thin film with a composition ratio of 45:45:10 for Al:Cr:Si in Ref. [79], revealing a fracture toughness of ~3.2 MPa·m^{1/2} before and after subjecting the thin film to a heating cycle up to 700°C. While Drnovšek *et al.* [79] saw a decrease of fracture toughness down to ~1.8 MPa·m^{1/2} during micromechanical cantilever testing up to 600°C, the value for K_{Ic} rose slightly to ~2.0 MPa·m^{1/2} when testing at 700°C. The fracture toughness even fully recovered, when testing at room temperature after heating, indicating the beneficial influence on Si on the microstructure. Comparably, Bartosik *et al.* reported K_{Ic} values of up to 3.0 ± 0.2 MPa·m^{1/2} in as-deposited TiSiN thin films with a nanocomposite microstructure [41], where the peak toughness was measured at 8.5 at.% Si. An enhanced fracture toughness through superlattice architectures was reported in Ref. [11], where the measured fracture toughness of 2.5 ± 0.1 MPa·m^{1/2} for

TiN/Cr_{0.37}Al_{0.63}N superlattices surpassed the K_{Ic} values of the monolithic TiN and Cr_{0.37}Al_{0.63}N thin films, which were 2.0 ± 0.1 and 1.3 ± 0.1 MPa·m^{1/2}, respectively. In Ti_{0.40}Al_{0.60}N thin films, K_{Ic} values of 3.0 ± 0.01 MPa·m^{1/2} were reported in Ref. [14] upon vacuum annealing at 900°C for 10 min, which decreased to 2.8 ± 0.4 MPa·m^{1/2} for an annealing temperature of 1000°C.

However, despite the previous efforts to increase the fracture toughness of protective TMN thin films, an examination of the load-displacement curves (if displayed) reveals that brittle failure occurred abruptly without any interruption. Even if the magnitude of the fracture toughness reported in this study may not be extraordinary high, the direct observation of the interrupted fracture process is unparalleled in the existing literature. The thin film design concept presented in this thesis uncovers a promising potential for the microstructural design of hard protective thin films with improved fracture properties.

5

Conclusions and outlook

The principal aim of this study was to explore the influence of microstructure, elemental composition and thermal history on the mechanical properties of AlCrSiN thin films. To achieve this, cathodic arc evaporation was used to deposit a multilayer film, consisting of ten sets of 250 nm thick sublayers of $\text{Al}_{0.63}\text{Cr}_{0.27}\text{Si}_{0.1}\text{N}$ alternated with 50 nm thick sublayers of $\text{Al}_{0.675}\text{Cr}_{0.075}\text{Si}_{0.25}\text{N}$. In addition, two monolithic thin films, sharing identical compositions with the intermittent sublayers of the multilayer film, were examined as reference materials.

Correlative SEM and TEM analysis revealed that the heat-treatment at 1050°C for 5 min effectively induced the formation of globular c-Cr(Al)N precipitates in the $\text{Al}_{0.63}\text{Cr}_{0.27}\text{Si}_{0.1}\text{N}$ thin film material, while $\text{Al}_{0.675}\text{Cr}_{0.075}\text{Si}_{0.25}\text{N}$ remained devoid of precipitates following the same heat-treatment. Consequently, in the heat-treated AlCrSiN multilayer this resulted in a cross-sectional occurrence of alternating sublayers with and without precipitates, respectively.

CSnanoXRD measurements unveiled a dual-phase nanocomposite microstructure, consisting of w-Al(Cr)N and c-Cr(Al)N nanocrystals with a size of ~5 nm. Residual stress analysis indicated that the heat-treatment led to a reduction in the compressive stresses present in both the monolithic and multilayer thin films, decreasing from about -7 to -3.5 GPa and from -6 to -2 GPa, respectively.

Within the multilayered thin film, this sequential variation of mechanical properties effectively facilitated extrinsic toughening, resulting in stepwise crack propagation observed during in situ microcantilever bending tests. The successful application of a toughening mechanism to the heat-treated AlCrSiN multilayer led to an increase in fracture toughness, reaching up to $2.7 \pm 0.2 \text{ MPa}\cdot\text{m}^{1/2}$, accompanied by a fracture stress of $4.9 \pm 0.5 \text{ GPa}$.

These findings revealed a unique mechanism for enhancing toughness, which is applicable to TMN thin films. This enhancement was achieved through a multifaceted approach, involving (i) a multilayer architectural design, (ii) a finely tuned AlCrSiN nanocomposite microstructure allowing for (iii) precipitation-based grain boundary design. Subsequent research endeavours will be directed towards refining the heat-treatment parameters and optimizing the multilayer morphology to fully harness the uncovered potential of this toughening concept.

Bibliography

- [1] L. Hultman, *Vacuum*, 2000, **57**, 1–30, DOI: 10.1016/S0042-207X(00)00143-3.
- [2] C. Mitterer, in *Comprehensive Hard Materials*, Elsevier Ltd, 2014, vol. 2, pp. 449–467, DOI: 10.1016/B978-0-08-096527-7.00035-0.
- [3] A. V. Pshyk, A. Vasylenko, B. Bakhit, L. Hultman, P. Schweizer, T. E. Edwards et al., *Materials & Design*, 2022, **219**, 110798, DOI: 10.1016/J.MATDES.2022.110798.
- [4] A. P. Serro, C. Completo, R. Colaço, F. dos Santos, C. L. da Silva, J. M. Cabral et al., *Surface and Coatings Technology*, 2009, **203**, 3701–3707, DOI: 10.1016/J.SURFCOAT.2009.06.010.
- [5] M. Wittmer, *Journal of Vacuum Science & Technology A*, 1985, **3**, 1797–1803, DOI: 10.1116/1.573382.
- [6] P. H. Mayrhofer, C. Mitterer, L. Hultman and H. Clemens, *Progress in Materials Science*, 2006, **51**, 1032–1114, DOI: 10.1016/J.PMATSCI.2006.02.002.
- [7] A. G. Evans, *Journal of the American Ceramic Society*, 1990, **73**, 187–206, DOI: 10.1111/J.1151-2916.1990.TB06493.X.
- [8] W. M. Seidl, M. Bartosik, S. Kolozsvári, H. Bolvardi and P. H. Mayrhofer, *Vacuum*, 2018, **150**, 24–28, DOI: 10.1016/j.vacuum.2018.01.028.
- [9] R. Daniel, M. Meindlhumer, W. Baumegger, J. Zalesak, B. Sartory, M. Burghammer et al., *Acta Materialia*, 2017, **122**, 130–137, DOI: 10.1016/J.ACTAMAT.2016.09.027.
- [10] R. Daniel, M. Meindlhumer, J. Zalesak, B. Sartory, A. Zeilinger, C. Mitterer et al., *Materials & Design*, 2016, **104**, 227–234, DOI: 10.1016/J.MATDES.2016.05.029.
- [11] J. Buchinger, A. Wagner, Z. Chen, Z. L. Zhang, D. Holec, P. H. Mayrhofer et al., *Acta Materialia*, 2021, **202**, 376–386, DOI: 10.1016/J.ACTAMAT.2020.10.068.
- [12] J. Buchinger, N. Koutná, Z. Chen, Z. Zhang, P. H. Mayrhofer, D. Holec et al., *Acta Materialia*, 2019, **172**, 18–29, DOI: 10.1016/J.ACTAMAT.2019.04.028.
- [13] M. Meindlhumer, T. Ziegelwanger, J. Zalesak, M. Hans, L. Löfler, S. Spor et al., *Acta Materialia*, 2022, **237**, 118156, DOI: 10.1016/j.actamat.2022.118156.
- [14] M. Bartosik, C. Rumeau, R. Hahn, Z. L. Zhang and P. H. Mayrhofer, *Scientific Reports 2017 7:1*, 2017, **7**, 1–9, DOI: 10.1038/s41598-017-16751-1.

- [15] D. G. Sangiovanni, V. Chirita and L. Hultman, *Thin Solid Films*, 2012, **520**, 4080–4088, DOI: 10.1016/J.TSF.2012.01.030.
- [16] H. Holleck and V. Schier, *Surface and Coatings Technology*, 1995, **76-77**, 328–336, DOI: 10.1016/0257-8972(95)02555-3.
- [17] F. Barthelat, H. Tang, P. D. Zavattieri, C. M. Li and H. D. Espinosa, *Journal of the Mechanics and Physics of Solids*, 2007, **55**, 306–337, DOI: 10.1016/J.JMPS.2006.07.007.
- [18] H. D. Espinosa, J. E. Rim, F. Barthelat and M. J. Buehler, *Progress in Materials Science*, 2009, **54**, 1059–1100, DOI: 10.1016/J.PMATSCI.2009.05.001.
- [19] P. Fratzl and R. Weinkamer, *Progress in Materials Science*, 2007, **52**, 1263–1334, DOI: 10.1016/J.PMATSCI.2007.06.001.
- [20] M. Meindlhumer, J. Zalesak, R. Pitonak, J. Todt, B. Sartory, M. Burghammer et al., *Nanoscale*, 2019, **11**, 7986–7995, DOI: 10.1039/C8NR10339A.
- [21] O. Kolednik, J. Predan, F. D. Fischer and P. Fratzl, *Advanced Functional Materials*, 2011, **21**, 3634–3641, DOI: 10.1002/ADFM.201100443.
- [22] R. Daniel, M. Meindlhumer, J. Zalesak, W. Baumegger, J. Todt, T. Ziegelwanger et al., *Materials & Design*, 2020, **196**, 109169, DOI: 10.1016/J.MATDES.2020.109169.
- [23] R. Hahn, M. Bartosik, R. Soler, C. Kirchlechner, G. Dehm and P. H. Mayrhofer, *Scripta Materialia*, 2016, **124**, 67–70, DOI: 10.1016/J.SCRIPTAMAT.2016.06.030.
- [24] W.-D. Münz, *Journal of Vacuum Science & Technology A*, 1986, **4**, 2717–2725, DOI: 10.1116/1.573713.
- [25] A. E. Reiter, V. H. Derflinger, B. Hanselmann, T. Bachmann and B. Sartory, *Surface and Coatings Technology*, 2005, **200**, 2114–2122, DOI: 10.1016/j.surfcoat.2005.01.043.
- [26] A. E. Reiter, C. Mitterer and B. Sartory, *Journal of Vacuum Science & Technology A: Vacuum, Surfaces, and Films*, 2007, **25**, 711–720, DOI: 10.1116/1.2738492.
- [27] S. Veprek and M. J. Veprek-Heijman, *Surface and Coatings Technology*, 2008, **202**, 5063–5073, DOI: 10.1016/j.surfcoat.2008.05.038.
- [28] M. Alfreider, M. Meindlhumer, T. Ziegelwanger, R. Daniel, J. Keckes and D. Kiener, *MRS Bulletin*, 2023, DOI: 10.1557/S43577-023-00549-W.
- [29] H. Willmann, P. H. Mayrhofer, P. O. Persson, A. E. Reiter, L. Hultman and C. Mitterer, *Scripta Materialia*, 2006, **54**, 1847–1851, DOI: 10.1016/J.SCRIPTAMAT.2006.02.023.

- [30] J. Soldán, J. Neidhardt, B. Sartory, R. Kaindl, R. Čerstvý, P. H. Mayrhofer et al., *Surface and Coatings Technology*, 2008, **202**, 3555–3562, DOI: 10.1016/J.SURFCOAT.2007.12.041.
- [31] Y. Makino and K. Nogi, *Surface and Coatings Technology*, 1998, **98**, 1008–1012, DOI: 10.1016/S0257-8972(97)00391-5.
- [32] P. H. Mayrhofer, H. Willmann and A. E. Reiter, *Surface and Coatings Technology*, 2008, **202**, 4935–4938, DOI: 10.1016/J.SURFCOAT.2008.04.075.
- [33] M. Kawate, A. Kimura and T. Suzuki, *Journal of Vacuum Science & Technology A*, 2002, **20**, 569–571, DOI: 10.1116/1.1448510.
- [34] N. Jäger, M. Meindlhumer, S. Spor, H. Hruby, J. Julin, A. Stark et al., *Acta Materialia*, 2020, **186**, 545–554, DOI: 10.1016/j.actamat.2020.01.026.
- [35] J. L. Endrino, S. Palacín, M. H. Aguirre, A. Gutiérrez and F. Schäfers, *Acta Materialia*, 2007, **55**, 2129–2135, DOI: 10.1016/J.ACTAMAT.2006.11.014.
- [36] W. Wu, W. Chen, S. Yang, Y. Lin, S. Zhang, T. Y. Cho et al., *Applied Surface Science*, 2015, **351**, 803–810, DOI: 10.1016/J.APSUSC.2015.05.191.
- [37] M. Hans, D. Music, Y. T. Chen, L. Patterer, A. O. Eriksson, D. Kurapov et al., *Scientific Reports 2017 7:1*, 2017, **7**, 1–7, DOI: 10.1038/s41598-017-16567-z.
- [38] P. H. Mayrhofer, R. Rachbauer, D. Holec, F. Rovere and J. M. Schneider, *Comprehensive Materials Processing*, 2014, **4**, 355–388, DOI: 10.1016/B978-0-08-096532-1.00423-4.
- [39] J. Schiøtz, T. Vegge, F. D. Di Tolla and K. W. Jacobsen, *Physical Review B*, 1999, **60**, 11971, DOI: 10.1103/PhysRevB.60.11971.
- [40] S. Veprek, H. D. Männling, M. Jilek and P. Holubar, *Materials Science and Engineering: A*, 2004, **366**, 202–205, DOI: 10.1016/J.MSEA.2003.08.052.
- [41] M. Bartosik, R. Hahn, Z. L. Zhang, I. Ivanov, M. Arndt, P. Polcik et al., *International Journal of Refractory Metals and Hard Materials*, 2018, **72**, 78–82, DOI: 10.1016/J.IJRMHM.2017.12.015.
- [42] J. Musil, J. Vlček and P. Zeman, <http://dx.doi.org/10.1179/174367508X306460>, 2013, **107**, 148–154, DOI: 10.1179/174367508X306460.
- [43] L. Castaldi, D. Kurapov, A. Reiter, V. Shklover, P. Schwaller and J. Patscheider, *Surface and Coatings Technology*, 2007, **202**, 781–785, DOI: 10.1016/J.SURFCOAT.2007.05.070.

- [44] Y. Moritz, C. Saringer, M. Tkadletz, A. Stark, N. Schell, I. Letofsky-Papst et al., *Surface and Coatings Technology*, 2020, **404**, 126632, DOI: 10.1016/J.SURFCOAT.2020.126632.
- [45] M. Ohring, *Materials Science of Thin Films, Deposition and Structure*, 2001, pp. 95–201.
- [46] T. Ziegelwanger, MA thesis, Montanuniversität Leoben, 2021.
- [47] C. A. Schneider, W. S. Rasband and K. W. Eliceiri, *Nature Methods* 2012 9:7, 2012, **9**, 671–675, DOI: 10.1038/nmeth.2089.
- [48] M. Stefenelli, J. Todt, A. Riedl, W. M. T. Ecker, R. Daniel, M. Burghammer et al., *J Appl Crystallogr*, 2013, **46**, 1378–1385.
- [49] J. Keckes, M. Bartosik, R. Daniel, C. Mitterer, G. Maier, W. Ecker et al., *Scripta Materialia*, 2012, **67**, 748–751, DOI: 10.1016/j.scriptamat.2012.07.034.
- [50] L. Spieß, G. Teichert, R. Schwarzer, H. Behnken and C. Genzel, *Moderne Röntgenbeugung*, Springer Spektrum, 2019, vol. 3.
- [51] C. Riekkel, M. Burghammer and R. Davies, *IOP Conference Series: Materials Science and Engineering*, 2010, **14**, 012013, DOI: 10.1088/1757-899X/14/1/012013.
- [52] J. Keckes, R. Daniel, J. Todt, J. Zalesak, B. Sartory, S. Braun et al., *Acta Materialia*, 2018, **144**, 862–873, DOI: 10.1016/J.ACTAMAT.2017.11.049.
- [53] J. Kieffer and J. P. Wright, *Powder Diffraction*, 2013, **28**, S339–S350, DOI: 10.1017/S0885715613000924.
- [54] J. Kieffer and D. Karkoulis, *Journal of Physics: Conference Series*, 2013, **425**, DOI: 10.1088/1742-6596/425/20/202012.
- [55] S. Bodner, P. Gawlitza, J. Holcova, M. Meindlhumer, Q. Nguyen, S. Niese et al., *European Synchrotron Radiation Facility*, 2026, DOI: data.esrf.fr/doi/10.15151/ESRF-ES-1176719961.
- [56] J. Keckes, A. Lassnig, M. Meindlhumer, J. Todt and T. Ziegelwanger, *European Synchrotron Radiation Facility*, 2025, DOI: data.esrf.fr/doi/10.15151/ESRF-ES-964909431.
- [57] M. Birkholz, *Thin film Analysis by X-ray Scattering*, Wiley-VCH, 2005.
- [58] P. Scherrer, *Nachrichten von der Gesellschaft der Wissenschaften zu Göttingen, Mathematisch-Physikalische Klasse*, 1918, **1918**, 98–100.
- [59] R. Daniel, K. J. Martinschitz, J. Keckes and C. Mitterer, *Acta Materialia*, 2010, **58**, 2621–2633, DOI: 10.1016/J.ACTAMAT.2009.12.048.

- [60] P. J. Withers and H. K. Bhadeshia, <http://dx.doi.org/10.1179/026708301101510087>, 2013, **17**, 366–375, DOI: 10.1179/026708301101510087.
- [61] J. Todt, J. Zalesak, C. Krywka and J. Keckes, *Advanced Engineering Materials*, 2021, **23**, DOI: 10.1002/ADEM.202100130.
- [62] M. M. Stefanelli, R. Daniel, W. Ecker, D. Kiener, J. Todt, A. Zeilinger et al., *Acta Materialia*, 2015, DOI: doi.org/10.1016/j.actamat.2014.11.011.
- [63] J. I. C. Noyan and B. Cohen, *Residual Stress: Measurement by Diffraction and Interpretation*, 1987.
- [64] B. J. Goodno and J. M. Gere, *Mechanics of Materials Ninth Edition*, Cengage Learning, 2018.
- [65] A. Riedl, R. Daniel, M. Stefanelli, T. Schöberl, O. Kolednik, C. Mitterer et al., *Scripta Materialia*, 2012, **67**, 708–711, DOI: 10.1016/j.scriptamat.2012.06.034.
- [66] D. Gross and T. Seelig, *Bruchmechanik Mit einer Einführung in die Mikromechanik*, Springer Vieweg, 2016.
- [67] M. Alfreider, S. Kolitsch, S. Wurster and D. Kiener, *Materials and Design*, 2020, **194**, 108914, DOI: 10.1016/j.matdes.2020.108914.
- [68] B. Biondi and S. Caddemi, *International Journal of Solids and Structures*, 2005, **42**, 3027–3044, DOI: 10.1016/j.ijsolstr.2004.09.048.
- [69] A. Alijani, M. Mastan Abadi, A. Darvizeh and M. K. Abadi, *Archive of Applied Mechanics*, 2018, **88**, 875–895, DOI: 10.1007/s00419-018-1347-0.
- [70] C. Tritremmel, R. Daniel, M. Lechthaler, P. Polcik and C. Mitterer, *Thin Solid Films*, 2013, **534**, 403–409, DOI: 10.1016/j.tsf.2013.03.017.
- [71] M. Pohler, R. Franz, J. Ramm, P. Polcik and C. Mitterer, *Surface and Coatings Technology*, 2011, **206**, 1454–1460, DOI: 10.1016/J.SURFCOAT.2011.09.028.
- [72] A. Khatibi, J. Sjölen, G. Greczynski, J. Jensen, P. Eklund and L. Hultman, *Acta Materialia*, 2012, **60**, 6494–6507, DOI: 10.1016/J.ACTAMAT.2012.08.010.
- [73] H. Köstenbauer, G. A. Fontalvo, M. Kapp, J. Keckes and C. Mitterer, *Surface and Coatings Technology*, 2007, **201**, 4777–4780, DOI: 10.1016/J.SURFCOAT.2006.10.017.
- [74] A. Jelinek, M. J. Pfeifenberger, R. Pippan and D. Kiener, *JOM*, 2021, **73**, 4248–4257, DOI: 10.1007/S11837-021-04963-W.

- [75] M. J. Pfeifenberger, M. Mangang, S. Wurster, J. Reiser, A. Hohenwarter, W. Pfleging et al., *Materials & Design*, 2017, **121**, 109–118, DOI: 10.1016/J.MATDES.2017.02.012.
- [76] A. O. Eriksson, J. Q. Zhu, N. Ghafoor, M. P. Johansson, J. Sjölen, J. Jensen et al., *Surface and Coatings Technology*, 2011, **205**, 3923–3930, DOI: 10.1016/J.SURFCOAT.2011.02.007.
- [77] M. Hans, M. to Baben, Y. T. Chen, K. G. Pradeep, D. M. Holzapfel, D. Primet-zhofer et al., *Surface and Coatings Technology*, 2016, **305**, 249–253, DOI: 10.1016/J.SURFCOAT.2016.08.046.
- [78] L. Rogström, N. Ghafoor, J. Schroeder, N. Schell, J. Birch, M. Ahlgren et al., *Journal of Applied Physics*, 2015, **118**, DOI: 10.1063/1.4927156.
- [79] A. Drnovšek, H. T. Vo, M. R. de Figueiredo, S. Kolozsvári, P. Hosemann and R. Franz, *Surface and Coatings Technology*, 2021, **409**, DOI: 10.1016/j.surfcoat.2021.126909.

List of Figures

2.1	Schematic overview of the sputter processes taking place at the target surface during cathodic arc evaporation, redrawn after [45].	7
2.2	Schematic representation of the three investigated thin films, note that this sketch is not true to scale. In the $\text{Al}_{0.63}\text{Cr}_{0.27}\text{Si}_{0.1}\text{N}$ thin film the heat-treatment leads to the formation of globular c-Cr(Al)N precipitates, while the second reference thin film $\text{Al}_{0.675}\text{Cr}_{0.075}\text{Si}_{0.25}\text{N}$ is expected to remain unaffected by the heat-treatment.	9
2.3	Constructive interference occurs when the path difference between two interfering waves is an integer multiple of the wavelength λ . Since the waves are elastically scattered, the wavelength remains constant. The right-hand figure shows the condition of interference transferred to reciprocal space. Diffraction is only recorded if the diffraction vector \vec{Q} is equal to the reciprocal space vector \vec{H}_{hkl} . \vec{k}_0 and \vec{k}_1 represent primary and secondary beam vectors, respectively.	11
2.4	CSnanoXRD setup shows the vertically oriented sample that is scanned across in transmissional geometry. The X-ray beam is focussed to a beam size of $\sim 75 \times 75 \text{ nm}^2$ using a pair of multilayer Laue lenses (MLLs). Debye-Scherrer ring with a diffraction angle of 2θ are collected by a 2D detector EigerX 4M.	13
2.5	The detector image was captured during a cross-sectional line scan through an as-deposited $\text{Al}_{0.63}\text{Cr}_{0.27}\text{Si}_{0.1}\text{N}$ thin film. In a 110 fibre textured thin film the intensity of the 100 Debye-Scherrer ring is increased at the azimuthal angles δ of about 30 and -30 deg.	15
2.6	Cross-section of the heat-treated multilayer sample polished by a focused ion beam. On top of the polished cross-section a protective deposited tungsten layer of $\sim 300 \text{ nm}$ is visible as a bright region.	17
2.7	Free-standing notched and unnotched microcantilevers are shown in the upper and lower picture, respectively. The geometry of the cantilever is described by the width B and thickness t . In case of the notched cantilever a is the notch depth. Length L corresponds to the testing length in the evaluation process. P indicates the force that is applied by the indenter in the bending tests.	18
2.8	A schematic stress distribution across an elastically loaded cantilever. . .	20

2.9	A representative cantilever of an as-deposited multilayer sample before (a), during (b) and after the bending test (c).	21
2.10	Upon crack propagation in a cantilever its stiffness is reduced. This allows for the analytical evaluation of crack lengths from the measured load-displacement curves.	25
3.1	SEM micrographs imaging of fracture cross-sections of the two reference thin films and the multilayer in the as-deposited (a, b, c) as well as heat-treated state (d, e, f). Please note that for (a) and (d), (b) and (e) as well as for (c) and (f) the same scale bar applies, respectively.	27
3.2	SEM images of FIB-polished cross-sections of the two reference thin films and the multilayer in the as-deposited (a, b, c) as well as heat-treated state (d, e, f). The scalebar applies to all images.	28
3.3	HAADF micrograph and elemental colour maps obtained by EDS mapping in TEM for the heat-treated $\text{Al}_{0.63}\text{Cr}_{0.27}\text{Si}_{0.1}\text{N}$ thin film in (a). The graph presented in (b) shows the elemental composition along the line that is oriented parallel to the film growth direction.	29
3.4	HAADF micrograph and elemental colour maps obtained by EDS mapping in TEM for the heat-treated $\text{Al}_{0.675}\text{Cr}_{0.075}\text{Si}_{0.25}\text{N}$ thin film are presented in (a). The elemental composition profiles along the lines 1 and 2, that are oriented perpendicular and parallel to the growth direction of the thin film, are presented in (b) and (c), respectively.	30
3.5	HAADF micrograph and elemental colour maps obtained by EDS mapping in TEM for the heat-treated multilayer are presented in (a). The graph in (b) shows the elemental composition along the line oriented parallel to the growth direction of the thin film.	31
3.6	HAADF micrograph and elemental colour maps for the multilayer received by EDS mapping conducted in TEM. The two graphs in (b) and (c) show the atomic contents along the respective lines in the micrograph (a).	31
3.7	HAADF micrograph and elemental colour obtained by EDS mapping in TEM for the heat-treated multilayer. The line shown in the TEM micrograph (a) was set to display the elemental composition across a precipitate in (b).	32

3.8	CSnanoXRD data retrieved from the as-deposited $\text{Al}_{0.63}\text{Cr}_{0.27}\text{Si}_{0.1}\text{N}$ film. In (a) the phase plot obtained by an azimuthal integration of the corresponding Debye-Scherrer rings is shown, while in (b) the azimuthal distribution of the diffracted intensities indicates a $\langle 110 \rangle$ fibre texture. From the cross-sectional variation in the FWHM of the AlN 100 peak a crystallite size of ~ 5 nm was calculated (c). The residual stress evaluated from the AlN 100 Debye-Scherrer ring shows an oscillatory variation around a mean value of ~ 7 GPa (d).	33
3.9	CSnanoXRD data retrieved from the heat-treated $\text{Al}_{0.63}\text{Cr}_{0.27}\text{Si}_{0.1}\text{N}$ film. In (a) the phase plot obtained by an azimuthal integration of the corresponding Debye-Scherrer rings is shown, while in (b) the azimuthal distribution of the diffracted intensities indicates $\langle 110 \rangle$ fibre texture. The cross-sectional FWHM variation of the AlN 100 peak is decreased with respect to the as-deposited thin film due to temperature-activated microstructural recovery processes (c). The residual stress evaluated from the AlN 100 Debye-Scherrer ring shows a variation around a mean value of ~ 3.5 GPa (d).	34
3.10	CSnanoXRD data retrieved from the as-deposited $\text{Al}_{0.675}\text{Cr}_{0.075}\text{Si}_{0.25}\text{N}$ film. In (a) the phase plot obtained by an azimuthal integration of the corresponding Debye-Scherrer rings is shown, while in (b) the azimuthal distribution of the diffracted intensities indicates $\langle 110 \rangle$ fibre texture. The cross-sectional FWHM of the AlN 100 peak reveals equiaxial nanocrystallites with a size of ~ 7 nm (c). The residual stress evaluated from the AlN 100 Debye-Scherrer ring shows an oscillatory variation around a mean value of ~ 7.5 GPa (d).	36
3.11	CSnanoXRD data retrieved from the heat-treated $\text{Al}_{0.675}\text{Cr}_{0.075}\text{Si}_{0.25}\text{N}$ film. In (a) the phase plot obtained by an azimuthal integration of the corresponding Debye-Scherrer rings is shown, while in (b) the azimuthal distribution of the diffracted intensities indicates $\langle 110 \rangle$ fibre texture. The cross-sectional FWHM of the AlN 100 peak is increased with respect to the as-deposited condition (c). The residual stress evaluated from the AlN 100 Debye-Scherrer ring shows an oscillatory variation in a range of ~ 4 to -3.5 GPa (d).	37

3.12	CSnanoXRD data retrieved from the as-deposited AlCrSiN multilayer thin film. In (a) the phase plot obtained by an azimuthal integration of the corresponding Debye-Scherrer rings is shown, while in (b) the azimuthal distribution of the diffracted intensities indicates no preferred orientation in the multilayer. The cross-sectional FWHM of the AlN 100 peak indicates uniform domain sizes in both sublayers (c). The residual stress evaluated from the AlN 100 Debye-Scherrer ring periodically varies between ~ 6 and ~ 5.5 GPa in the thicker and thinner sublayer, respectively (d).	38
3.13	CSnanoXRD data retrieved from the heat-treated AlCrSiN multilayer thin film. In (a) the phase plot obtained by an azimuthal integration of the corresponding Debye-Scherrer rings is shown, while in (b) the azimuthal distribution of the diffracted intensities texture remained inconclusive. The cross-sectional FWHM of the AlN 100 peak indicates uniform domain sizes in both sublayers (c). The residual stress evaluated from the AlN 100 Debye-Scherrer ring shows an oscillatory variation around a mean value of ~ 2 GPa (d).	39
3.14	Results from microcantilever bending tests for the $\text{Al}_{0.63}\text{Cr}_{0.27}\text{Si}_{0.1}\text{N}$ monolithic thin film calculated from the load-displacement data. In (a), the applied stress-displacement curves obtained from two representative unnotched cantilevers both for as-deposited and heat-treated conditions are shown, while in (b) the applied K_I -displacement for representative notched cantilevers in both sample conditions is displayed.	40
3.15	Results from microcantilever bending tests for the $\text{Al}_{0.675}\text{Cr}_{0.075}\text{Si}_{0.25}\text{N}$ monolithic thin film calculated from the load-displacement data. In (a), the applied stress-displacement curves from two representative unnotched cantilevers are presented for both as-deposited and heat-treated conditions, while in (b) the applied K_I -displacement for representative notched cantilevers in both sample conditions is displayed.	41
3.16	Results from microcantilever bending tests for the multilayer. In (a) the maximum applied tensile stress-displacement curves, which were obtained from unnotched cantilevers, are shown. Stress intensity-displacement curves, that were retrieved from notched cantilevers, are plotted in (b). In both graphs, representative curves are shown for both the as-deposited and heat-treated conditions.	42

3.17	Fracture surfaces of unnotched (a, b) and notched (c, d) $\text{Al}_{0.63}\text{Cr}_{0.27}\text{Si}_{0.1}\text{N}$ cantilevers imaged <i>ex situ</i> in the SEM after the bending tests. The length of the scale bars in (a-c) corresponds to 500 nm.	44
3.18	Fracture surfaces of unnotched (a, b) and notched (c, d) $\text{Al}_{0.675}\text{Cr}_{0.075}\text{Si}_{0.25}\text{N}$ cantilevers imaged <i>ex situ</i> in the SEM after the bending tests. The length of the scale bars in (a-c) corresponds to 500 nm	45
3.19	Fracture surfaces of unnotched (a, b) and notched (c, d) AlCrSiN multilayer cantilevers imaged <i>ex situ</i> in the SEM after the bending tests. The scale bar applies to all micrographs.	46
3.20	Load-displacement curves recorded during the <i>in situ</i> bending tests on notched microcantilevers of the heat-treated AlCrSiN multilayer thin film. Clearly visible in all three depicted curves are discontinuities where the linearly progressing curve exhibits a drop in load. After the load drop, the slope is also decreased for all three load-displacement curves.	47
3.21	Load-displacement curves recorded during microcantilever bending tests of the heat-treated AlCrSiN multilayer thin film are depicted with a focus on the region where the load drop is observed. Prior to the significant load drop that leads to an intermittence in the load-displacement curve (encircled for notched cantilever 1), minor load drops are observed in (a) which are attributed to the failure of notch bridges. Due to a non-perfect sample fabrication and cantilever loading, the two bridges do not break at the exact same load. The shaded area marks the region where a linear fit of the curve was carried out in order to determine k_1 and k_2 , the stiffness of the notched microcantilever before and after the load drop, respectively.	48
3.22	The fracture surface of the microcantilever was imaged <i>ex situ</i> in the SEM. At several positions the notch depth and the distance from the notch tip to the interface of the low Si-containing interface was measured (a). The mean value is interpreted as Δa_{image} . The analytical solution as described in Sec. 2.6.5 correlates the crack length a to the stiffness k and allows for an evaluation of $\Delta a_{analytical}$ (b). In this case the cantilever thickness t was $2.69\ \mu\text{m}$, k_0 was calculated from a Young's modulus of $\sim 280\ \text{GPa}$ that was determined in bending tests on unnotched cantilevers.	49

3.23 Following the bending tests, the crack lengths of three notched cantilevers for the heat-treated multilayer were evaluated both analytically and from fracture surfaces. The results from both approaches are in good agreement and indicate stepwise crack propagation and a concomitant increase in fracture toughness. The graph in (b) shows a crack propagation resistance curve, also known as *R-curve*, with a rising $K-\Delta a$ behaviour. 50

List of Tables

2.1	An overview of the three deposited thin films and the applied annealing conditions. Altogether six sample types were analysed in this thesis. . . .	9
3.1	Mechanical properties of the $\text{Al}_{0.63}\text{Cr}_{0.27}\text{Si}_{0.1}\text{N}$ thin film evaluated from bending tests on unnotched and notched cantilevers.	41
3.2	Mechanical properties of the $\text{Al}_{0.675}\text{Cr}_{0.075}\text{Si}_{0.25}\text{N}$ thin film evaluated from bending tests on unnotched and notched cantilevers.	42
3.3	Mechanical properties of the multilayer thin film evaluated from microcantilever bending tests on unnotched and notched cantilevers.	43
3.4	Evaluated crack propagation for the three notched cantilevers of the heat-treated AlCrSiN multilayer.	49